Insight into a rift volcanism with the petrogenesis of ultramafic enclaves and the host basalts: Kula Volcanic Field, Western Anatolia, Turkey

Erdal Şen, Erkan Aydar, Pınar Şen, Alain Gourgaud

Insight into a rift volcanism with the petrogenesis of ultramafic enclaves and the host basalts: Kula Volcanic Field, Western Anatolia, Turkey

Journal:	*Italian Journal of Geosciences*
Manuscript ID	IJG-2022-1058.R2
Manuscript Type:	Original Article
Date Submitted by the Author:	n/a
Complete List of Authors:	Şen, Erdal; Hacettepe University, Geological Engineering Aydar, Erkan; Hacettepe University, Geological Engineering Şen, Pınar; General Directorate of Mineral Research and Exploration Gourgaud, Alain; Université Blaise-Pascal
Keywords:	Alkaline basalt, ultramafic enclaves, fractional crystallisation, partial melting, uplift

Insight into a rift volcanism with the petrogenesis of ultramafic enclaves and the host basalts: Kula Volcanic Field, Western Anatolia, Turkey

Erdal Şen[1*], Erkan Aydar[1], Pınar Şen[2] & Alain Gourgaud[3]

[1]*Hacettepe University, Dept. of Geological Engineering, Beytepe, Ankara, Turkey, 06800*

[2]*General Directorate of Mineral Research and Exploration, Mineral Research and Exploration Department, 06800, Çankaya/Ankara, Turkey*

[3]*Univérsité Blaise-Pascal, UMR-CNRS 6524, Campus Universitaire des Cézeaux, 6 Avenue Blaise Pascal, TSA 60026 - CS 60026- 63178, Aubiere Cedex, France*

EŞ, 0000-0002-9172-9926; EA, 0000-0002-6550-0714; PŞ, 0000-0002-2457-7280

*Corresponding author e-mail: erdals@hacettepe.edu.tr

ABSTRACT

The Quaternary Kula Volcanic Field (KVF), located on an E-W trending Plio-Quaternary horst, consists of at least 80 scoria cones, associated fissural lava flows and maars. Volcanic activity is divided into three main stages as BI (ca. 2-0.9 Ma), BII (ca. 300-50 ka) and BIII (ca. 10-0.7 ka). The volcanic products of BII and BIII contain ultramafic enclaves. They are generally spherical or elliptical varying in size from <1 to <48 cm and some samples bear vesicles and glass. Based on modal mineralogy, the dominant enclave types are hornblendite, Cpx-hornblendite, while Phl-clinopyroxenite, wehrlite, plagioclase-bearing Cpx-hornblendite and Hbl-gabbro are subordinate. They occasionally represent adcumulate and/or mesocumulate textures. The alkaline host rocks are basanite, phonotephrite, trachybasalt, picrobasalt, and foidite in composition.

LILE (Rb, Ba, Sr, and Pb) and HFSE (Nb, Ta) concentrations of host rocks indicate an Enriched Within Plate Mantle source. Additionally, they have high Nb/La (>1.3), Nb/Y (>1.7), and Nb/U (>31) ratios, reflecting that crustal contamination is insignificant. Petrogenetic modelling shows that Kula enclaves and host rocks are probably originating from 3-5% partial melting of garnet and spinel-peridotite mantle source mixtures. Rb/Sr (0.03-0.10) and slightly high Ba/Rb (9.5-23) ratios for host rocks demonstrate the presence of amphibole and phlogopite in their source, while low Rb/Sr (0.01-0.09) and high Ba/Rb (18-115) reveal

that amphibole is present in the source. Estimated T/P conditions of early crystallizations are between 19.5–9.5 kbar, 63–31 km, and 1260–1130 °C for host rocks and 18.3–11.1 kbar, 59–36 km, and 1324–1208 °C for the enclaves, which suggests that the crystallization might have taken place in the lithospheric mantle.

KEYWORDS: Alkaline basalt, ultramafic enclaves, fractional crystallisation, partial melting, uplift

1. INTRODUCTION

Anatolia is located in the collision zone between African-Arabian and Eurasian plates. The convergence began in the Late Cretaceous–Eocene and ended with the continental collision in the middle Miocene (Şengör & Yılmaz, 1981; Yılmaz et al., 1987; Ring & Layer, 2003; Okay. et al., 2010). This collision led to the Anatolian plate moving westwards via the North Anatolian and East Anatolian faults (Fig. 1a) (Dewey & Şengör, 1979; Şengör, 1979; Şengör & Yılmaz, 1981; Pasquaré et al., 1988; McKenzie, 2020; Şengör & Yazıcı, 2020; Seyitoğlu et al., 2022). The combined effects of the westward Anatolian migration, back-arc extension of Hellenic arc and the retreat of the trench are the main controls on subsequent expansion (Seyitoğlu & Scott, 1991, 1992; Seyitoğlu et al., 2002; Sözbilir, 2002; Westaway et al., 2005; Koçyiğit, 2005; Bozkurt & Mittwede, 2005; Ersoy & Helvacı, 2007; Jolivet et al., 2013; Gessner et al., 2013, 2018; Seyitoğlu et al., 2022). After crustal extension, metamorphic basement rocks of the Menderes Massif exhumed by a combination of west-east strike-slip faulting and successive north-south detachment faults (Bozkurt & Park, 1997; Bozkurt, 2001; Seyitoğlu, 1997; Lips et al., 2001; Gessner et al., 2001; Ring & Layer, 2003; Işık et al., 2004; Sözbilir, 2005; Bozkurt & Rojay, 2005; Ersoy et al., 2011, 2012). Gessner et al. (2013, 2018) divide the exhumation of the Menderes Massif into two stages as a resulting from of asthenospheric flow below western Anatolia. The rapid tectonic denudation was due to differential footwall uplift during the early Miocene, and the formation of the Central Menderes Metamorphic Core Complex (CMCC; 'inner' axial zone) by late Miocene to recent detachment fault and normal fault systems, located between northern and southern (Çine) segments of the complex (Fig. 1b). The Menderes Massif includes the NE-SW trending Miocene Gördes, Demirci, Selendi, and Uşak-Güre basins in its northern part (Seyitoğlu & Scott, 1991; Seyitoğlu & Scott, 1994; Helvacı, 1995; Helvacı & Yağmurlu, 1995; Seyitoğlu, 1997; Yılmaz et al., 2000; Bozkurt, 2003; Purvis & Robertson, 2004; Westaway et al., 2004; Erkül et al., 2005; Ersoy & Helvacı, 2007; Ersoy et al., 2010; Karaoğlu et al., 2010; Ersoy et

al., 2011, 2012). These basins were cut by seismically active E–W-trending oblique-normal faults, resulting in the formation of the Simav and Gediz grabens under the late Miocene to recent N-S rift-type extensional tectonics (Seyitoğlu, 1997; Cohen et al., 1995; Bozkurt & Sözbilir, 2004; Rojay et al., 2005; Emre & Sözbilir, 2007; Çiftçi & Bozkurt, 2009; Ersoy et al., 2010, 2011, 2012; Hakyemez et al., 2013; Hetzel et al., 2013) (Fig 1b).

Volcanism in NE-SW trending basins has been associated with lithospheric thinning, and the volcanic products show geochemical variations during Miocene, including high-K calc-alkaline felsic and shoshonitic, ultrapotassic-lamproitic rocks (early Miocene); high-K calc-alkaline intermediate and high-Mg shoshonitic to ultrapotassic rocks (middle Miocene); and K-trachybasaltic rocks (late Miocene) (Yılmaz, 1989, 1990; Seyitoğlu, 1997; Bunbury et al., 2001; Erkül et al., 2005; Innocenti et al., 2005; Westaway et al., 2006; Ersoy et al., 2008; Karaoğlu et al., 2010; Çoban et al., 2012; Prelevic et al., 2012). The Kula Volcanism (KVF), located within the Selendi Basin, began with eruptions of plateau lavas ~1.5-2 Ma ago and continued until prehistoric time as monogenetic volcanoes (Bunbury, 1996; Bunbury et al., 2001; Innocenti et al., 2005; Westaway et al., 2004, 2006). The KVF is characterized by high-Na alkaline volcanics in the rift-mode extension regime (Bunbury et al., 2001; Alıcı et al., 2002; Bozkurt & Sözbilir, 2004; Innocenti et al., 2005).

The KVF comprises 92 Quaternary monogenic volcanic centres (scoria cones, spatter cones, maars) and covers an area of around 350 km^2. The volcanic products contain ultramafic and mafic enclaves, which were previously studied by Hollnes et al. (2005), Hollnes & Bunbury (2006) and Grützner et al. (2013). Their previous studies mainly focused on hornblendite and clinopyroxenite samples. In this study, we also examine olivine-rich clinopyroxenite and wehrlite samples to demonstrate the origin of those co-genetic inclusions in the host basaltic rocks and their petrological importance.

2. CRUSTAL EXTENSION AND UPLIFT

It is generally accepted that Western Anatolian crust has experienced extension since the late Miocene to Pliocene (e.g. Angelier et al., 1981). Geophysical studies indicate that the crust's thickness in the west, near recent Kula alkaline basaltic volcanic area, is approximately 30 km, increasing to 34-38 km eastwards (Saunders et al., 1998; Zhu et al., 2006; Mahatsente et al., 2017). The active faults point out an extending subcrustal lithosphere as a result of mantle uplift in the region (Saunders et al., 1998). Basin sedimentation characteristics constrain uplift rates to 0.1 mm/year, for a period 2-0.2 Ma, followed by 3.5 mm/year (since 0.2 Ma) (Bunbury et al., 2001). Alternatively, erosion is estimated to be 0.1 mm/year, with a total amount of uplift ~ 410 m since 3.1 Ma (Westaway et al., 2006). In addition, Bunbury et al. (2001) suggest that the presence of the Hbl-dominant mafic-ultramafic enclaves in the BII Kula lavas is a magmatic evidence supporting the “uplift” model. Doglioni et al. (2002) proposed that the last activity of the KVF rapidly erupted in a strongly extensional regime during neotectonic period due to the “horizontal windows” resulting from the tearing of the Aegean and Cyprus slabs ~20 Ma ago, which allowed the asthenospheric inflow into the lithosphere. However, the interaction of the asthenospheric mantle upwelling with the lithosphere is controversial. Two hypotheses have been proposed to explain lithospheric thinning and its relation to adiabatic upwelling of the asthenosphere. The first one is the transformation of the lower parts of the lithosphere into asthenosphere (asthenospherisation), resulting in the reconstruction of the paleo-depth of the Menderes lithospheric root (Prelevic et al., 2012). The second hypothesis is the delamination of lithospheric mantle by loss of material owing to gravitational collapse (Seyitoğlu & Scott, 1996; Aldanmaz et al., 2000; Ersoy et al., 2008, 2011; Karaoğlu et al., 2010). Geophysical studies support a lithospheric thinning in western Anatolia around Menderes Massif. A low-velocity zone (ca. 80 km depth) underlying a thin lithosphere has been found near the KVF (Salaün et al., 2012; Mahatsente et al., 2017). Most of the western Anatolia has an anomalously thin (50-80 km) and hot lithosphere that is possibly thinned to the crust (ca. 60

km, i.e. ~30 km below from the Moho) corresponding to the depth of basaltic magma generation (Artemieva & Shulgin, 2019).

3. GEOLOGICAL BACKGROUND

The bedrocks underlying the KVF comprise Palaeozoic-Triassic metamorphic units (schist, gneiss, and serpentinite), Cretaceous ophiolite mélange (ultramafic rocks, listvenite), and 800 m thick Miocene-Pliocene sedimentary rocks (claystone, siltstone, sandstone, conglomerate and lacustrine limestone) (Ercan et al., 1978).

Ercan et al. (1983) proposed three volcanic stages, while Bunbury (1996) and Bunbury et al. (2001) identified four episodes of the KVF. In this study, we divided the KVF into three volcanic stages: BI, BII, and BIII, based on the stratigraphical, morphological and chronological data (Fig. 2).

3.1. First Stage *(BI)*:

The BI volcanics outcrop in the eastern part of the study area. K-Ar and Ar-Ar radiometric data plot between 0.99 ±0.11 – 1.94 ±0.16 Ma (Fig. 2: Bunbury et al., 2001; Westaway et al., 2004, 2006; Maddy et al., 2015). The stage is primarily effusive, and its lavas flow over the Neogene sediments. They form a flat hat in the topographic heights, and the erosion of the concerned sediments, particularly in Gediz River gorge, formed spectacular earth pillars or fairy chimneys. Those lava flows cover an area of about 35 km^2, and their thickness ranges from 5 to 25 m.

3.2. Second Stage *(BII)*:

This stage comprehends the predominant volcanic activities of the KVF, represented by 49 cinder cones and associated lava flows, 3 tuff rings and 1 maar. K-Ar and Ar-Ar radiometric data of the BII basalts have ages ranging from 50 ±9 to 300 ±3 ka (Fig. 2: Bunbury et al.,

2001; Westaway et al., 2004, 2006). They outcrop in topographically lowlands compared to BI and are more altered than BI lava flows. Onion-skin alterations are commonly observed at the lava fronts. We encountered evidence of hydromagmatic activities only in this stage. The base surge deposits surrounding the crater comprise ash and lapilli layers, dune, anti-dune structures and bomb sags (Fig. 3a). Kızıl Tepe tuff ring (M3) deposits contain ultramafic enclaves.

3.3. Third Stage *(BIII)*:

There are 31 cinder cones associated with at least 28 individual lava flows. In the west of the study area, lavas flowed down southwestward about 17 km (Fig. 2). BIII lava flows are a′a type and distinct with their fresh black-coloured appearance, sharp-edged blocks, and unvegetated cover. BIII cinder cones can also easily be distinguished from BII cinder cones due to their lower erosion, steeper slopes, clearly visible craters and lack of soil covers. We also distinguished 16 small cinder cones (without crater) forming a cluster at the north of Divlit Tepe near Kula, where there is the source area for the BIII lavas reaching the Gediz River (Fig. 2, 3b). Most of the cinder cones are breached by lava flows, as shown in Figure 3c. Fissures and fractures are occasionally well-expressed by the spatter cones and tumuli. The volcanic products of BIII are the youngest of the KVF eruptions, with radiometric ages spanning between 0.7 ±0.4 and 10.6 ±1.9 ka (Westaway et al., 2004, 2006; Heineke et al., 2016; Ulusoy et al., 2019). Human footprints are well known on the basaltic base surge deposits near the Lake of Demirköprü Dam, and Ulusoy et al. (2019) have determined an age of 4.7 ±0.5 ka for these footprints using cosmogenic ^{36}Cl and combined U-Pb and (U-Th)/He zircon double-dating methods.

4. ENCLAVES

The lavas and cinder projections contain mafic and ultramafic enclaves varying in size from <1 to 48 cm. They are absent in the BI lava flows, but they are generally observed within the

ejecta of cinder cones, maars (Fig. 3a, d) and rare lava flows of the latest stage (BIII). The lava flows originating from the breached Bağ Tepe cinder cone are rich in enclaves (Fig. 3e, f). The most characteristic feature of Kula enclaves is the presence of vesicular glass (Fig. 3g). Most of the enclaves are rounded and sub-rounded with a smooth surface. Apart from these enclaves, foliated metamorphic (mica schist and mica gneiss etc.) and magmatic xenoliths are also present in the ejecta. In contrast to magmatic enclaves, they have an angular shapes and irregular surfaces.

5. ANALYTICAL TECHNIQUES

Electron microprobe analyses of the cores and rims of phenocrysts, microcrysts, microlites and glass were performed by Cameca SX100 instrument at the Blaise-Pascal University, France. Operating conditions were: 15 kV accelerating voltage, 10–12 nA current and 10 s counting time for each element.

Bulk-rock major and trace element analyses were performed at the Geological Engineering Department of Hacettepe University, Turkey, using a Philips PW 1480 X-Ray Fluorescence spectrometer, from fused glass tablets and pressed powdered samples. Alıcı et al. (1998) gave a detailed explanation of sample preparation. The spectrometer was calibrated using international standards (USGS and GEOSTANDARTS) to ensure accurate data. The X-ray Fluorescence spectrometer was calibrated by using USGS and Geostandards to ensure accurate data. Rare earth element (REE) analyses were performed by a JY701 inductively coupled plasma emission spectrometer at the Blaise Pascal University in Clermont-Ferrand, France.

6. PETROGRAPHY

6.1. Host rock

Lava samples from the KVF are typically porphyritic, with groundmass textures ranging from intergranular to intersertal. Many lavas show obvious petrographic evidence of disequilibrium, including strongly resorbed phenocrysts, reaction rims, zoned minerals, disequilibrium mineral assemblage, and compositions. The main phenocryst phases are olivine, clinopyroxene and hornblende, with plagioclase, leucite, and nepheline being less abundant than mafic minerals. Mineral abbreviations are from Whitney & Evans (2010).

*Olivine (*Ol*)* is the most abundant phenocryst phase in BI basalt, ranging from 4 to 10 vol.% of the rock. Olivines occasionally exhibit strongly skeletal texture in the BI and BIII basalts and are frequently euhedral, sub-rounded (Fig. 4a-c). The iddingsite sparsely replaced olivine in the groundmass of BI basalt.

*Clinopyroxene (*Cpx*)* is the most dominant mineral in all stages. They are euhedral, subhedral, rounded, and strongly zoned (Fig. 4c). Some clinopyroxenes exhibit zoning, especially in BI and BII basalts. The core zone, green in colour, is usually resorbed and surrounded by colourless outer rim (Fig. 4e).

*Hornblende (*Hbl*)* is present only in the BII and BIII stages. They are prismatic, locally resorbed (BIII), and generally rimmed by opaque oxides (BII) (Fig. 4c-d). We observed a cumulate texture consisting of hornblende assemblage in BIII basalt (Fig 4f).

*Plagioclase (*Pl*)* is microlitic commonly with rare phenocrysts in all stages. They show some disequilibrium features, such as honeycomb texture with numerous glass inclusions, fresh core with dusty zone rims, and resorption.

Nepheline is commonly present as microlite in the groundmass of the BIII basalt. *Leucite* is abundant in the lavas of the BIII, with a high modal percentage (up to %19), and sporadically represented in the crystal aggregates (Fig. 4c).

Fe-Ti Oxides exist in the groundmass as titanomagnetite and spinel microphenocrysts in BIII stage. It is also observed in the form of inclusions in olivine, clinopyroxene and leucite (Fig. 4b, d).

6.2. Enclaves

Ultramafic and mafic enclaves are observed in BII and BIII stages. Modal results are as follows: Cpx-hornblendite (12), hornblendite (8), Pl bearing Cpx-hornblendite (6), wehrlite (6), Ol-Hbl-clinopyroxenite (5), Hbl-gabbro (4) and phlogopite (Phl) clinopyroxenite (1) (Fig. 5). Glass and vesicle abundances are highly variable among the enclaves (Suppl. Table 1), reaching up to 48%. Enclaves are observed not only as hand specimens, but also as micro-enclaves, including interstitial glass in thin sections (Fig. 4f-h).

6.2.1. Hornblendites: Cpx-Hornblendite (BII), Hornblendite (BII, BIII), Pl-Bearing Cpx-Hornblendite (BIII)

Cpx-hornblendites and hornblendites generally exhibit porphyritic texture. The relationships among grains are largely intergranular and sub-ophitic with interstitial vesicular glass (Fig. 6a-c). They are essentially composed of long prismatic hornblendes (Fig. 6i). One of the Cpx-hornblendites contains pale blue hauyne minerals in a pocket of vesicular glass (Fig. 6d). Hornblendes commonly have fresh cores but altered rims. Some of them are resorbed and contain glass inclusions.

Apart from the porphyritic texture, plagioclase-bearing Cpx-hornblendites occasionally present adcumulate and/or mesocumulate textures with sporadically pegmatitic appearance. They bear glass, resorbed hornblende, rounded clinopyroxene, ragged phlogopite and resorbed plagioclase. Some plagioclase and apatite minerals also contain glass inclusions (Fig. 6e).

6.2.2. Clinopyroxenites: Phl-Clinopyroxenite (BIII) and Ol-Hbl-Clinopyroxenite (BII)

We have only one Phl-clinopyroxenite sample. It consists of strongly resorbed phlogopite (<12 mm, vol.38.5% modal) and subhedral resorbed clinopyroxene (vol.33% modal) with

interstitial vesicular glass (vol.25% modal). This enclave exhibits well developed embayment textures of phlogopite (Fig. 6f).

Ol-Hbl-clinopyroxenite enclaves (up to 7% Ol, 21% Hbl) show well-defined adcumulate texture (Fig. 6j). They mainly consist of subhedral, sub-rounded pale green coloured clinopyroxene and reddish-brown-coloured hornblende with intercumulus resorbed phlogopite and apatite (Fig. 6j). Several samples contain coarse-grained clinopyroxene (ca. 1-14 mm) replaced by hornblende along cleavage planes (Fig. 6k). Olivine is sub-rounded and iddingsite is observed along its cracks (Fig. 6k).

6.2.3. Hbl-Gabbro (BIII)

These are represented by fine grained (<1 mm), resorbed, prismatic, greenish-brown and acicular hornblende, minor embayed olivine and dusty-rimmed plagioclase (Fig. 6l-m). Phlogopite only occurs around olivine (Fig. 6m).

6.2.4. Wehrlite (BII)

Wehrlite enclaves have poikilitic textures of strongly resorbed hornblende and sub-rounded, partially resorbed olivine (1-7 mm) in clinopyroxene (<14 mm) oikocrysts (Fig. 6g, h). Some have orthocumulate textures comprised of euhedral-subhedral olivine (62–68%), interstitial subhedral clinopyroxene (Fig. 6n). Minor phlogopite grains formed around olivine and hornblende in contact with glass. Apatite is accessory and only found in glass. Additionally, euhedral Cr-spinel is found in olivine as inclusions (Fig. 6g).

7. MINERAL COMPOSITIONS

7.1. Olivine

Phenocryst and microcryst are variable in composition (Fo_{70-87}) (Suppl. Table 2). Compositional zoning is more pronounced in enclaves (especially in wehrlite) than in the

host rock, but some grains are slightly richer in Fe. In contrast to wehrlite, the olivine gabbro Mg number (Mg#) values range from 80 to 85.

7.2. Clinopyroxene

Selected analyses are listed in Supplementary Table 3. Endmember plots in Figure 7 (Morimoto, 1988) for host rock and enclave minerals show that all pyroxene is diopsitic (Wo_{46-57}, En_{20-45}, Fs_{6-30}), except two clinopyroxene analyses in host rock. One of them has spongy texture, and the other is reversely zoned with hedenbergitic composition. The Mg# of clinopyroxene slightly decrease from phenocryst (92) to microcryst (55) in the host rocks. The compositional range is wide and noticeable variations in Mg#, Al_2O_3 and TiO_2 content have been detected, particularly in BII and BIII basalt. In contrast to BII and BIII, BI clinopyroxenes have lower Al (<6%) and Ti content (<2%).

7.3. Amphibole

The chemical composition of hornblendes is summarised in Supplementary Table 4. They are conspicuously rich in TiO_2. According to Leake et al. (1997), the host rock amphiboles are mostly kaersutite with rare pargasite. Pargasites contain lower K_2O, TiO_2, Mg# and higher CaO content than the kaersutite composition. Some reversely zoned hornblendes exist in GIII basalt with Mg enrichment at the rim of phenocrysts.

Amphiboles in the enclaves are pargasitic and kaersutitic. The Mg#s range between 57 and 77. Some microcrysts in the glass and inclusions have lower Mg# (52-62). Amphiboles in the enclaves are generally Mg-rich in their core, except those in wehrlite. Moreover, amphiboles in the Hbl-Gabbro have lower Mg# compared to those of the other enclaves.

7.4. Phlogopite

Phlogopite is only seen in Hbl-gabbro, Phl-clinopyroxenite and rarely in wehrlite. Analyses are listed in Supplementary Table 5, with Fe# ranging from 0.17 to 0.29 (Rieder et al., 1998, Fe# < 0.3). Phlogopite in Phl-clinopyroxenite has higher Fe, Al, Ti and lower Na content compared to phlogopite in Hbl-gabbro.

7.5. Plagioclase

The selected analyses are presented in Supplementary Table 6. In the host rock, plagioclases (An_{46_64}) are mostly andesine, with rare labradorite. Some microlites exhibit higher An content than the unstable phenocrysts (anal. #2b). In Hbl-gabbro, the plagioclase composition is relatively andesine (An_{43-47}), but in Cpx-hornblendite, they represent an extensive compositional variation (An_{60-94}), ranging from labradorite to pure anortite. Some plagioclases in Cpx-hornblendite are resorbed and contain glass inclusions.

7.6. Feldspathoids

The representative analyses are given in Supplementary Table 7. The *nepheline* of the BII stage has slightly higher Al_2O_3, FeO, CaO and lower Na_2O than the nepheline of the BIII. In the enclave, nepheline is only observed in Hbl-clinopyroxenite (BII) and exhibits compositional similarity with those of the BII stage.

Hauyne occurs exclusively in the Cpx-hornblendite (Fig. 6d, BII), with K_2O and Na_2O content changing from 4.3 to 6.3% and from 7.3 to 10.3%, respectively.

7.7. Oxides

Ti-magnetite is present as microcrysts in groundmass and inclusion phases in all the three generations of the basalt. The chemical composition of Ti-magnetite is very homogeneous, containing approximately 22-23% TiO_2 (Suppl. Table 8).

Al-spinels have bimodal distribution in the host rock BIII, occurring as euhedral microphenocrysts and inclusion in olivine and leucite phenocrysts. The microphenocryst Al-spinel is more evolved, with a lower Mg# than the inclusions.

Cr-spinel is observed as inclusion and is only present in wehrlite sample, with the Cr# (Cr/(Cr+Al)) changing from 25 to 36.

Mg-ilmenite is only observed in Cpx-hornblendite samples, containing 7-8% MgO, 33-34% FeO and 53-54% TiO_2.

7.8. Vesicular Glass

The ratio of the glass and vesicles within the enclaves is highly variable (Suppl. Table 1). The glass in the enclaves of the BII stage varies in volume from 0.3 to 19%, while those of BIII range from 9 to 29%. The glass exhibits a variety of colours ranging from light brown, reddish dark brown to black, but the glass in the Hbl-gabbro is commonly colourless. Two types of glasses, similar to those identified by Yaxley et al., (1997), have been observed in the enclaves, namely “glass pocket” (Gp), and “glass associated with intergranular minerals” (Gim). The Gp is occasionally observed in the enclaves of the BII stage, which modally comprise less than 15 vol.% of the glass. In some of the Ol-Hbl-clinopyroxenite and wehrlite samples, the Gps are frequently connected with a glass film, forming a network system (Fig. 6j, n). However, the Gim is commonly found in the hornblendite, Cpx-hornblendite, and Phl-clinopyroxenite samples, mostly belonging to BIII stage (Fig. 6a-d, f, i). In several enclaves, the Gp consists of disequilibrium mineral assemblage, such as resorbed minerals (hornblende, olivine, phlogopite, apatite and hauyne) (Fig. 6d, f-h). Some minerals have reacted with glass, resulting in a dark-coloured contact surface between mineral and melt, observed in both the glass veins and glass pockets (Fig. 6g-j). Relict fragments of phlogopite, completely surrounded by the glass, are optically continuous with larger primary phlogopite (Fig. 6f). The glass in the coarse-grained enclaves, especially hornblendites,

comprise euhedral and prismatic apatites (Fig. 6b-e, h, j). They are observed as both isolated crystals and inclusions in hornblende and clinopyroxene.

The glass contains a high concentration of vesicles, with the abundance of the vesicles occasionally surpassing that of the glass content. The vesicles typically increase in size from the Gim (<0.1 mm) to Gp (<1.5 mm). They are mostly spherical to elliptical in the Gp, in contrast to those in the Gim. Some vesicle walls in the glass are collapsed or probably plucked out during thin-section preparation (Fig. 6c).

The chemical composition of the glasses is given in Supplementary Table 9. The glasses are intermediate to basic (44-56 wt.% SiO_2), and are commonly foiditic, phonotephritic, and rarely tephriphonolitic and basanitic (Fig. 8). The glass in the enclaves relatively comprises higher SiO_2 and total alkaline content than their bulk rock. The glasses with the lowest SiO_2 content (44-47%) occur in wehrlite, Phl-clinopyroxenite, and a Cpx-hornblendite. Although the enclaves have different mineralogy and chemistry, Figure 9 shows that the composition of the glass from wehrlite to Hbl-gabbro samples exhibits evident trends on the plots of SiO_2 versus major oxides. Some glass composition within Phl-clinopyroxenite does not conform to the general trends. Glass adjacent to phlogopite is commonly rich in K_2O, Na_2O and Al_2O_3 and poor in MgO and CaO.

8. GEOCHEMISTRY

Major oxides, trace, and rare element compositions of representative samples from Kula lava flows and their enclaves are listed in Supplementary Table 10. All samples exhibit an alkaline trend (Fig. 8). The *BI* lava flows range in composition from basanite, trachybasalt and phonotephrite. While the majority of the samples from *BII* host rocks are basanite with lesser amount of phonotephrite, *BIII* host rocks are phonotephrite in composition. Besides, although enclaves are mantle rocks and should not be shown on the TAS diagram with host volcanics, they are plotted on the same diagram to show similarities or variations in chemical

compositions. Enclaves are definitely ultrabasic in character, with SiO_2 (39-45%) and K_2O+Na_2O (1-7.5 %) values, lower than their host rocks.

Plots of SiO_2 versus selected major oxides are shown in Figure 9. Increasing SiO_2 is well correlated with; i) decreasing Fe_2O_3, MgO, CaO, P_2O_5 and TiO_2 in both host rocks and their enclaves; ii) increasing Al_2O_3, Na_2O and K_2O in host rocks. However, Al_2O_3, Na_2O and K_2O contents of enclaves vary within a narrow range with no systematic variation (Fig. 9). The decrease in Fe_2O_3, MgO, CaO, P_2O_5, and TiO_2 is coherent with crystallisation of olivine, clinopyroxene, plagioclase, Fe-Ti oxides, and apatite.

The variations of Al_2O_3 and Na_2O in host rocks are notably different from those in their enclaves. As shown in Figure 9, while the Al_2O_3 and Na_2O contents of the host rocks increase with increasing SiO_2, the values of these elements decrease with increasing SiO_2 content in enclaves. This indicates that the Al_2O_3 contents increase from ultrabasic enclaves to basic host rocks, which may be linked to the plagioclase fractionation.

Trace element data are reported in Supplementary Table 10 and plotted against SiO_2 in Figure 9. The best correlation is represented by Co, V, Rb, and Sr. Ba, Nb, Y, and Zr show no systematic variation. The contents of Co and V regularly decrease with increasing SiO_2, possibly indicating the fractionation of olivine, spinel/clinopyroxene and V-bearing Fe-Ti oxides. On the other hand, Rb and Nb contents increase with increasing SiO_2.

MORB-normalised (Pearce, 1983) spider diagrams are shown in (Fig. 10). All samples from host rocks exhibit typical within-plate patterns (humped-patterns) enriched in large ion lithophile elements (LILE, e.g. Sr, K, Rb, Ba and Th), light rare earth elements (LREE), and high field strength elements (HFSE, e.g. Nb, Ta and Ti) relative to the MORB (Fig. 10a).

The trace element abundances of enclaves are characterized by significant depletion in Rb, K and Th with respect to HFS elements (Fig. 10b). The Kula enclaves are strongly depleted in Rb and Th compared to their host rocks. As expected, the enclave of Phl- clinopyroxenite (K97-70a2) show anomalously high K, Rb and Ba peaks.

REE data of both Kula host rocks and enclaves are summarized on a chondrite-normalised (Nakamura, 1974) diagrams. Both suites exhibit light LREE enrichment relative to chondrite (i.e. La= 70 to 250 times) and also show clear fractionation between LREE and HREE.

All samples for Kula host rocks have flat patterns from Er to Lu with respect to LREE (Fig. 10c). While the abundances of LREE are variable, the HREE are relatively constant. Herewith, LREE/HREE ratios are also variable, and the (La/Yb)n ratios of Kula host rocks range from 13.36 to 24.56.

Enclaves of Phl-clinopyroxenite (K97-70a2), Cpx-hornblendite (K97-30a, K97-48a2), hornblendite (K97-14a, K97-17a2) and plagioclase bearing Cpx-hornblendite (K97-46a) have almost similar patterns identical to those of host rocks (Fig. 10d). They are also characterized by LREE enrichment relative to chondrite (i.e. La= 70-250 times chondrite). However, they have more fractionated nature relative to their host rocks with (La/Yb)n ratios varying from 9.27 to 33.83. The wherlite sample (K97-10a2) also exhibits REE pattern similar to other enclaves but has considerably lower REE contents.

9. DISCUSSION AND CONCLUSION

9.1. Source Characteristics and Partial Melting Modeling

The ratio plots of alkaline elements, such as Ba, Rb and Sr, are used to detect the presence of amphibole and/or phlogopite in the source region of Kula host rocks and enclaves. These minerals are essential for revealing the metasomatic enrichment process in the source region since amphibole and/or phlogopite are major volatile bearing phases (Ionov et al., 1997). Furthermore, the presence of apatite crystals in the Kula enclaves also supports the metasomatism process. Yaxley et al. (1991) have demonstrated that the abundances of apatite may be attributed to the metasomatism. If relatively low-temperature melting conditions prevailed (e.g., 1100°C) in H_2O-bearing depths of the upper mantle, the residual

apatite could form (Watson, 1980). Rb and Ba, both are compatible with phlogopite (Kd_{Rb} and Kd_{Ba} are 3.06 and 1.090, respectively), whereas amphibole does not retain Rb, Sr and Ba (Kd_{Rb}= 0.29; Kd_{Ba}=0.42 and Kd_{Sr}=0.46) (Furman & Graham, 1999; Rollinson, 1993). Ionov & Hofmann (1995) have also indicated from the mantle xenoliths that amphibole has very low Rb concentrations while phlogopite is rich in Rb. According to these criteria, melting of an amphibole-bearing mantle source can reveal lower Rb/Sr and higher Ba/Rb ratios. Conversely, melts from phlogopite-bearing mantle sources (amphibole-free) may have higher Rb/Sr (>0.1) and lower Ba/Rb (<20) ratios than those formed from amphibole-bearing sources (Furman & Graham, 1999).

The alkaline host rocks have generally relatively low Rb/Sr (0.03-0.10) and high Ba/Rb (9.48-23.24) ratios (Fig. 11a), suggesting the presence of mostly amphibole with lesser amount of phlogopite in their source region. They also plot close to the trend line of amphibole and phlogopite. At the same time, the Rb/Sr and Ba/Rb ratios of Kula enclaves show wide variation and range from 0.01 to 0.09 and 17.57 to 114, respectively. The majority of the samples are clearly plotted on the amphibole trend line. As expected, the enclave of K97-70a2 (Phl-clinopyroxenite) is shifted towards the phlogopite trend line due to its relatively high Rb/Sr and low Ba/Rb ratios.

Furthermore, the high Na_2O/K_2O ratios (>1.27) of both Kula host rocks and enclaves (except sample no: K97-70a2, Phl-clinopyroxenite) further support the above arguments, as melting of amphibole bearing phases can account for Na_2O/K_2O>1 (Foley et al., 1999; Moufti et al., 2012).

To specify the source mineralogy and melting depth of Kula enclaves and their host rocks, partial melting modelling using REE ratios was calculated. The modelling uses the non-modal batch melting equations of Shaw (1970), partition coefficients from McKenzie & O'Nions (1991) and Rollinson (1993). Partial melting calculations were carried out by the "PETROMODELER" program of Ersoy (2013). In the calculations, LREE-enriched

compositions from McDonough (1990) were regarded as initial source composition. Spinel and garnet mineral modes were used to make an assessment of the melting depth (Baker et al., 1997; Shaw et al., 2003). LREE/HREE variations are good proxies for the depth/extent of melting and the residual garnet in the source. Garnet retains the HREE, and garnet-facies melts are represented by higher LREE/HREE ratios relative to spinel-facies. Figures 11b-d display Sm/Yb versus La/Yb variations for Kula host rocks and enclaves with non-modal batch melting curves of spinel and garnet peridotite sources. As expressed in Figure 11b, the genesis of Kula host rocks cannot be explained by variable degrees of melting from a single garnet or spinel peridotitic source. Thus, binary mixing calculations of Langmuir et al. (1978) were performed between spinel and garnet peridotite. Kula host basalts clearly plot on the lines obtained by binary mixing between 3-5% spinel and garnet peridotite melts. The mixing proportions extend between 40%-60% melt of spinel peridotite and 30%-70% melt of garnet. On the other hand, enclaves shifted towards the melting curve of garnet-facies.

Figure 11c illustrates the (Tb/Yb)n versus (La/Yb)n variations in Kula host rocks and enclaves with the horizontal line separating the garnet and spinel peridotite melting fields (Wang et al., 2002; 2004; Furman et al., 2004; Moufti et al., 2012). The (Tb/Yb)n ratios of Kula host rocks (1.50-2.03) are generally clustered on the horizontal line, indicating that melts originate from both garnet and spinel bearing sources, and extend along the mixing lines between 3% and 5% melt of garnet and 5% melt of spinel-peridotite. Calculations further support that the mixing of melts derived from both garnet and spinel peridotite sources accounts for the generation of Kula volcanism. Alıcı et al. (2002) have also suggested a mixture of asthenospheric and lithospheric mantle sources. Grützner et al. (2013) mention Mg-rich and green-core Mg-poor clinopyroxene in lava flows and enclaves indicating two different melt sources. In addition, Nikogosian et al. (2018) note that the compositional diversity of the Kula volcanism based on olivine-hosted melt inclusions indicates mixing of two distinct sources originated from the mantle, and the primary melt

generation starts from 75 km depth. However, according to Sölpüker (2007) Kula volcanism originates from spinel peridotite with 7–9% degrees of fractional melting.

As can be seen in Figures 11b-c, Kula enclaves are separated from their host rocks due to their relatively higher (Tb/Yb)n ratios (1.96-3.20), suggesting the presence of residual garnet and melting in garnet stability field (Wang et al., 2002; Khudoley et al., 2012). Variations in Sm/Yb, La/Yb Tb/Yb ratios in enclaves generally result from the melting of a garnet peridotite. If this is the case, we should not expect any variation in La/Yb and Yb diagram (Fig. 11d). However, the host rocks and enclaves have variation between La/Yb and Yb, further suggesting the mixing between spinel and garnet peridotite sources. Moreover, the presence of amphibole suggests the contribution of a spinel peridotite mantle source (Worthing & Nasir, 2008; Tschegg et al., 2011; Moufti et al., 2012).

9.2. Fractional Crystallisation and Crustal Contamination

Various types of enclaves varying from wehrlite to gabbro, indicate that magma masses had sufficient time for mineral settling to form cumulates. The melts reaching volatile saturation contributed to the formation of ultramafic cumulates of different mineralogical composition. For example, early-crystallized minerals such as spinel, olivine and clinopyroxenes produced wehrlite with subsiding evolved melts and hydrous fluids could activate the crystallisation of hornblende and phlogopite, producing hornblendites from primitive basaltic magma with Na-alkaline affinity. The presence of nepheline and hauyne in the BII stage's enclaves may indicate a magmatic evolution towards alkaline compositions.

The linear correlations between SiO_2 and some specific major and trace elements are consistent with fractional crystallisation processes in the evolution of Kula host basalts and enclaves. This could be explained by the presence of mafic microcrysts occurring in the vesicular glass. Low Ni (<106 ppm) and Cr (<205 ppm) contents in host basalts also support the arguments of fractional crystallization, as the decrease of Ni and Cr suggests olivine and

clinopyroxene fractionation, respectively (Wilson, 1989; Moufti et al., 2012). Furthermore, Ni and Cr contents of basalts (Ni: 7-106 ppm; Cr: 2-205 ppm) and enclaves (Ni: 0.5-91 ppm; Cr: 7-301 ppm) are lower than the values commonly accepted for primary magmas (Ni=300-400 ppm; Cr: 300-500 ppm; Jung & Masberg, 1998), possibly reflecting their fractionated nature [with the exception of one sample, wehrlite, which has high Ni (598 ppm) and Cr values (2331 ppm)]. For instance, the negative correlation between SiO_2 and MgO, Fe_2O_3, TiO_2, and CaO, coupled with some specific elements such as Co, V and Sr are indicative of olivine, clinopyroxene, Ca-plagioclase and Fe-Ti-oxides fractionation. P_2O_5 also has a clear negative correlation with SiO_2, which is consistent with apatite removal. The increasing trends between SiO_2 and K_2O, Na_2O and Rb also indicate fractional crystallisation processes in the evolution of Kula host basalts.

Haase et al. (2000) argue that a high Nb/La (>1) ratio is the striking feature of uncontaminated magmas from within-plate mantle sources. According to this criterion, it suggests that the host basalts, having elevated Nb/La ratios (>1.3), were derived from mantle sources with insignificant crustal contamination. Similarly, Nb/La ratios of the enclaves (Nb/La: 1.2-2.4) also resemble those of their host rocks from within-plate settings. Besides, Kula basalts and their enclaves have high Nb/Y ratios (>1.7), suggesting HFSE enrichment commonly seen in lavas uncontaminated by crustal material from within-plate mantle sources. This is a typical characteristic of uncontaminated alkaline ocean island basalts (Pearce & Cann, 1973). Alıcı et al. (2002) illustrated in the OIB-normalised spider diagram that the trace element patterns of Kula basalts are akin to OIB with considerable enrichment in LILE (e.g. Sr, Rb, Ba, K) and HFSE (e.g. Nb, Th, U). This case can be ascribed to mantle source enrichment during their genesis. The alkaline rocks studied here have enriched incompatible element characteristic with high Nb/La and Nb/Y ratios, suggesting derivation from a within-plate mantle source with an inconsequential crustal contamination. Likewise, the Nb/U ratio of uncontaminated OIB is around 47±10 (Hofmann et al., 1986); the

range in Nb/U (31-58) of Kula basalts rule out the significant role of crustal contamination. This argument is in agreement with the assessments of Güleç (1991) and Alıcı et al. (2002), who suggested based on their isotopic data that Kula host rocks have not been subjected to notable crustal contamination but have been treated by the effects of fractional crystallization. Tokçaer et al. (2005) and Agostini et al. (2007) also suggest an OIB-like asthenospheric mantle source for the KVF, without any contamination. The rapid ascent of magma in Kula (Tokçaer et al., 2005) and short residence time in the crust (Georgatou & Chiaradia, 2020) explain the negligible role of crustal contamination. This argument relates to the residence duration of basaltic magmas in the continental crust. According to Holness & Bunbury (2006), the co-genetic enclaves occur in the magma chamber emplaced beneath the KVF but in the crust. However, Spera (1984); Aldanmaz et al. (2005); Demouchy et al. (2006); Tang et al. (2006); Davis et al. (2007); Meng et al. (2015) and (Sun et al., 2018) suggest that the presence of xenoliths and/or xenocrysts implies rapid ascent of magmas without significant interaction with the crust. As the melts containing comagmatic enclaves rise into the crust after extraction from the magma chambers in the lithospheric mantle, the exsolution of volatiles increases, resulting in bulk magma volume expansion and the demolition of the conduit wall-rock (Sun et al., 2018). This process explains the abundance of the crustal xenoliths, such as granite, marble, schist, gneiss and migmatite, in the volcanic deposits of the KVF. Crustal xenoliths having low-temperature minerals in the Kula lavas and pyroclastics (Bayhan et al., 2002) suggest rapid ascent, thus avoiding remarkable assimilation with crustal materials. These views are further supported by the presence of embayed crystals indicating rapid changes in P-T conditions of magma batches. For instance, embayed phlogopite, hornblende and olivine crystals are observed in Phl-clinopyroxenite and wehrlite in Kula (Fig. 6). These embayed minerals may occur as a result of partial melting of hydrous minerals due to decompression (Green et al., 1968; Francis, 1987; Grützner et al., 2013). In addition, the release of exsolved fluids from ascending

magma within the cumulate mush may also lead to reactions with pre-existing crystals and producing hydrous phases such as phlogopite microcrysts mantling the olivine, observed in BIII basalt. Furthermore, the presence of glass, including merged vesicles, implies that enclaves experienced a decrease in pressure as the magma ascends rapidly to the surface. Grützner et al. (2013) calculated the ascent rate of the magma from Moho to surface as 4–11 days.

9.3. Thermobarometry

The textural properties indicate that the lava and enclaves may have a simple history of cooling and heating before reaching the surface. Fresh and stable mineral assemblages were selected, which were in equilibrium with the host magma. Clinopyroxene is ubiquitous in both host rocks and enclaves. The crystallisation temperature and pressure of clinopyroxene were estimated on the basis of Putirka (2008) equation 33, and Neave & Putirka (2017), respectively. The whole rock and glass compositions were regarded as liquid compositions, and the tests for equilibrium based on Putirka (1999) has been employed to get more plausible estimates from Cpx-thermometer model (Fig. 12).

Therefore, only the Cpx compositions having $K_D^{(Fe\text{-}Mg)}$ values between 0.20 and 0.36 that fell within the expected equilibrium range [$K_D^{(Fe\text{-}Mg)}$ =0.28±0.08] based on Putirka (2008), and the values (the difference between predicted and observed DiHd) approaching zero, were used. The diagram given here covers only predicted and observed DiHd (diopside+hedenbergite) components, with the one-to-one line having an accepted deviation of 10% (Mollo et al., 2015; Polo et al., 2017) (Suppl. Table 11).

Cpx-liquid (whole rock composition) thermobarometer yields the crystallisation temperature and pressure for BI, BII and BIII lava flows at 1217-1231°C (average of 1227°C) and 9.5-10.0 kbar (average of 9.8 kbar), 1130-1242°C (average of 1208°C) and 9.5-15.4 kbar

(average of 12.8 kbar) and 1149-1227°C (average of 1193°C) and 9.4-14.3 kbar (average of 12.7 kbar), respectively (Suppl. Table 11).

Cpx-liquid thermobarometry was used for the enclaves, based on both Cpx-whole rock and Cpx-co-existing glass pairs. Temperature and pressure estimates, based on the compositions of Cpx and co-existing glass, give the following values: 1138-1200°C, 14.2-18.8 kbar for wehrlite; 1148-1199°C, 25.2-27.6 kbar for Phl-clinopyroxenite; 1134-1206°C, 14.4-21.4 kbar for Cpx-hornblendite; and 1026-1034°C, 14.2-15.7 kbar for Hbl-gabbro. However, estimates based on Cpx-whole rock composition yield higher temperatures but lower pressures relative to the Cpx-glass composition pairs. In other words, temperature and pressure estimates based on Cpx and co-existing glass compositions indicate the different source regions. The inconsistency between the probable source characteristics might originate from the analysed glasses, resulting from decompression-induced partial melting of hydrous minerals such as amphibole and phlogopite (Fig. 6f-h).

BI basalts are the first products of the Kula volcanism, which developed as a result of crustal thinning caused by mantle uplift in the Selendi basin on horst about 1.2 Ma ago. P-T calculations indicate shallower sources (~ 30-36 km) for BI stage compared to other stages. The BII and BIII stages have relatively the deeper origins. As the heat from the upwelling asthenosphere rises (Prelevic et al., 2012), it might produce the initial melts of the spinel-bearing BII and BIII basalts. Thus, the depth of the partial melting point may shift to a deeper source from 30 to 50 km (Fig. 12). Most of the enclaves ranging from Phl-bearing wehrlite to hornblendite are found in the base surge deposits of the M3 tuff ring (BII). In contrast to lava flows of the BI and BIII stages, the P-T analyses of the Cpx minerals of a fusiform bomb covering the wehrlite yield crystallisation temperatures of 1174-1260°C and pressures of 13-19.5 kbar, which corresponds to depths of ~42-63 km in the lithosphere. These depths are generally compatible with the T-P conditions of the enclaves.

The ascending melts needs to stall at depths of the lithospheric mantle to form various ultramafic enclaves. So, the alkaline basaltic melts, enriched with volatiles, migrate upwards from the source region by percolating into the lithosphere to form a magma storage such as small magma chambers and/or feeder dykes (Grützner et al., 2013) or lens-shaped masses (i.e. “sill-like” Hollnes & Bunbury, 2006). According to P-T graph (Fig. 12), the magma storage depths calculated from Cpx-liquid (whole rock composition) are between about 38-59 km for hornblendite (BII), 46-50 km for Phl-clinopyroxenite (BII), 39-48 km for Cpx-hornblendite (BII), and 36-42 km for Hbl-gabbro (BIII). The melting temperature notably controls the MgO and Al_2O_3 content of a melt (Pilet et al., 2010). High TiO_2 (1.81-4.19 wt.%), Al_2O_3 (14.6-18.2 wt.%) and low MgO (5.4-12.1 wt.%) contents point out the involvement of a non-peridotite source, possibly an amphibole-bearing pyroxenite. Residual amphibole can be attributed to melting near the asthenosphere-lithosphere boundary and/or under lithospheric conditions (Mayer et al., 2013), since amphibole is not stable above ~100 km (Pilet et al., 2008). The calculated pressures correspond to depths of approximately 36 to 63 km, suggesting the crystallisation under lithospheric mantle conditions.

In the light of the data, the evolution of Kula volcanism resulting from asthenospheric uplift can be summarized as follows (Fig. 13):

I. Kula host basalts and enclaves most likely originated from a mixed garnet and spinel peridotite source in the presence of amphibole and lesser phlogopite, indicating metasomatic enrichment processes during their genesis.

II. The Kula Rift Volcanism is a sodic alkaline volcanism developed within the Gediz Graben of the Western Anatolian Graben system. The first basaltic phase started to produce lava flows about 1.2 Ma ago. These lava flows are cut by normal faults in the form of staircases after settling and descending into the graben. Although Richardson-Bunbury (1996) obtained Ar-Ar ages from the amphiboles of these lava flows, we did not encounter any minerals indicating the presence of aqueous phases in these lavas

during our extensive sampling. Our clinopyroxene geobarometer calculations indicate that the crystallization occurred at a depth of 30-36 km, which is the lower crust and lithospheric mantle transition level. We did not encounter any basic or ultrabasic enclaves in these basaltic lava flows that were formed during a dry phase. Therefore, we accept that these lavas originated from sub-crustal magma settlements, which probably also contributed to the uplift.

III. The petrographic and compositional study of the enclaves has shown that Kula enclaves record multistage fractional crystallisation histories involving the migration of melts and aqueous fluids from asthenosphere and/or lithosphere-asthenosphere interaction levels. Wehrlite, Cpx-hornblendite, and hornblendite enclaves are abundant in the second phase-basalts. According to geobarometer calculations, the crystallization depths of these enclaves are between 40-55 km, while Cpx from host basalts exhibits a wide range of crystallization depths, as 38-60 km. While Cpx-hornblendite, hornblendite, and Hbl-gabbro enclaves are commonly encountered in the third-stage basalts, the crystallization depths obtained from these enclaves indicate shallower depths (35-43 km) compared to other stage enclaves.

IV. The most striking features of enclaves are that they are as fresh as the host rock, show no deformation, and contain vesiculated interstitial glass. With these features, we can say that enclaves and host basalts originated from the same source and rose rapidly with the lava. As the phases progress from the second to the third stage, magma chambers in the lithospheric mantle get closer to the surface.

V. The tectonic regime that created the rift is still active, and considering the very young products of the third phase, we suggest that a volcanic eruption may occur in the near future.

ACKNOWLEDGEMENTS

This research was supported by TÜBİTAK (Scientific and Technical Research Council of Turkey), within the cadre of project YDABCAG-398, the Scientific Research Unit of Hacettepe University (project T07 604 002) and by the French Embassy in Ankara (French Ministere des Afaires Etrangéres). Part of this research is compiled from the PhD thesis of Erdal Şen. We are grateful to anonymous reviewers for their constructive comments which greatly improved the manuscript. We extend our special appreciation to Editor Dr. Federico Rossetti for his expertise and attention.

REFERENCES

Agostini S., Doglioni, C., Innocenti F., Manetti P., Tonarini S., Savaşçin M.Y. (2007) – The transition from subduction-related to intraplate Neogene magmatism in the Western Anatolia and Aegen area. In Beccaluva, L., Bianchini, G., and Wilson, M., eds., Cenozoic Volcanism in the Mediterranean Area: Geological Society of America Special Paper 418, 1–15, https://doi.org/10.1130/2007.2418(01)

Aldanmaz E., Gourgaud A., Kaymakcı N. (2005) - Constraints on the composition and thermal structure of the upper mantle beneath NW Turkey: Evidence from mantle xenoliths and alkali primary melts. J. Geodyn., 39, 277-316. https://doi.org/10.1016/j.jog.2005.01.002

Aldanmaz E., Pearce J. A., Thirlwall M.F., Mitchell J.G. (2000) - Petrogenetic evolution of late Cenozoic, post-collision volcanism in western Anatolia, Turkey. J. Volcanol. Geotherm., 102, 67-95.

Alıcı P., Temel A., Gourgaud A. (2002) - Pb-Nd-Sr isotope and trace element geochemistry of Quaternary extension-related alkaline volcanism: a case study of Kula region (western Anatolia, Turkey). J. Volcanol. Geotherm., 115, 487-510.

Alıcı P., Temel A., Gourgaud A., Kiefer G., Gündoğdu M.N. (1998) - Petrology and geochemistry of potassic rocks in the Gölcük area (Isparta, SW Turkey): genesis of enriched alkaline magmas. J. Volcanol. Geotherm., 85, 423–446.

Angelier J., Dumont J. F., Karamanderesi H., Poisson A., Simsek S., Uysal S. (1981) - Analyses of fault mechanism an expansion of southwestern Anatolia since the Late Miocene. Tectonophysics, 75, T1-T9.

Artemieva I.M. & Shulgin A. (2019) - Geodynamics of Anatolia: Lithosphere thermal structure and thickness. Tectonics, 38, 4465-4487. https://doi.org/10.1029/2019TC005594

Baker J.A., Menzies M.A., Thirlwall M.F., Macpherson C.G. (1997) - Petrogenesis of Quaternary intraplate volcanism, Sana'a, Yemen: implications for plume–lithosphere interaction and polybaric melt hybridization. J. Petrol., 38, 1359–1390.

Bayhan H., Aydar E., Şen E. Gourgaud A. (2006) - Melting of crustal xenoliths within ascending basalt: Example from the Kula volcanic field, western Anatolia, Turkey. C. R. Geosci., 338/4, 237-243.

Bozkurt E. (2001) - Neotectonics of Turkey—a synthesis. Geodin. Acta, 14, 3–30.

Bozkurt E. (2003) - Origin of NE-trending basins in western Turkey, Geodin. Acta, 16, 2–6, 61-81. https://doi.org/10.1016/S0985-3111(03)00002-0.

Bozkurt E. & Park R. (1997) - Microstructures of deformed grains in the augen gneisses of southern Menderes Massif (western Turkey) and their tectonic significance. *Geol Rundsch,* 86**,** 103–119. https://doi.org/10.1007/s005310050125

Bozkurt E. & Sözbilir H. (2004) - Tectonic evolution of the Gediz Graben: field evidence for an episodic, two stage extension in western Turkey, Geol. Mag., 141, 63-79.

Bozkurt E. & Mittwede S. (2005) - Introduction: Evolution of continental extensional tectonics of western Turkey. Geodin. Acta, 18, 153-165. 10.3166/ga.18.153-165.

Bozkurt E. & Rojay B. (2005) - Episodic, two-stage Neogene extension and short-term intervening compression in Western Turkey: field evidence from the Kiraz Basin and Bozdağ Horst, Geodin. Acta, 18:3-4, 299-316, DOI: 10.3166/ga.18.299-316

Bunbury J.M.R. (1996) - The Kula Volcanic Field, western Turkey: the devolopment of a Holocene alkali basalt province and the adjacent normal-faulting graben. Geol. Mag., 133 (3), 275-283

Bunbury J.M., Hall L., Anderson G.J., Stannard A. (2001) - The determination of fault movement history from the interaction of local drainage with volcanic episodes. Geol. Mag., 138, 185-192

Cohen H.A., Dart C.J., Akyüz H.S., Barka A.A. (1995) - Syn-rift sedimentation and structural development of the Gediz and Büyük Menderes grabens, western Turkey. J. Geol. Soc., London 152, 629-638.

Çiftçi B. & Bozkurt E. (2009) - Pattern of normal faulting in the Gediz Graben, SW Turkey. Tectonophysics, 473, 234-260. https://doi.org/10.1016/j.tecto.2008.05.036

Çoban H., Karacık Z. Ece Ö.I. (2012) - Source contamination and tectonomagmatic signals of overlapping Early to Middle Miocene orogenic magmas associated with shallow continental subduction and asthenospheric mantle flows in Western Anatolia: A record from Simav (Kütahya) region. Lithos, 140-141, 119-141.

Davis A.S., Clague D.A., Paduan J.B. (2007) - Diverse Origins of Xenoliths from Seamounts at the Continental Margin, Offshore Central California. J. Petrol., 48 (5), 829-852.

Demouchy S., Jacobsen S. D., Gaillard F., Stern C. R. (2006) - Rapid magma ascent recorded by water diffusion profiles in mantle olivine. Geology, 34, 429–432.

Dewey J.F. & Şengör A.M.C. (1979) - Aegean and surrounding regions: complex multiplate and continuum tectonics in a convergent zone. Geol. Soc. Amer. Bull., 90, 84-92.

Doglioni C., Agostini S., Crespi M., Innocenti F., Manetti P., Riguzzi F., Savasçı Y. (2002) - On the extension in western Anatolia and the Aegean Sea. J. Virtual Explor., 8,169-183. https://doi.org/10.3809/jvirtex.2002.00049

Elkins L.J., Gaetani G.A., Sims K.W.W. (2008) - Partitioning of U and Th during garnet pyroxenite partial melting: Constraints on the source of alkaline ocean island basalts, Earth Planet. Sci. Lett., 265, 1–2, 270-286. https://doi.org/10.1016/j.epsl.2007.10.034

Emre T. & Sözbilir H. (2007) - Tectonic evolution of the Kiraz Basin, Küçük Menderes Graben: evidence for compression/uplift-related basin formation overprinted by extensional tectonics in West Anatolia. Turk. J. Earth Sci., 16, 441–470.

Ercan T., Dinçel A., Metin S., Türkecan A., Günay E. (1978) - Uşak yöresindeki Neojen havzaların jeolojisi. TJK Büll., c.21, 97-106.

Ercan T., Türkecan A., Dinçel A., Erdoğdu G. (1983) - Kula-Selendi (Manisa) Dolaylarının Jeolojisi. Jeoloji Müh. Derg., 173-28.

Erkül F., Helvacı C., Sözbilir H. (2005) - Evidence for two episodes of volcanism in the Bigadic borate basin and tectonic implications for western Turkey. Geol. J., 40, 545–570.

EROS (2018) - Shuttle Radar Topography Mission (SRTM) 1 Arc-Second Global. Earth Resources Observation and Science Center (EROS). U.S. Geological Survey. https://doi.org/10.5066/F7PR7TFT

Ersoy E.Y. (2013) - PETROMODELER (Petrological Modeler): A Microsoft® Excel© spreadsheet program for modeling melting, mixing, crystallisation and assimilation processes in magmatic systems. Turk. J. Earth Sci., 22, 115-125.

Ersoy Y. & Helvacı C. (2007) - Stratigraphy and geochemical features of the Early Miocene bimodal (ultrapotassic and calc-alkaline) volcanic activity within the NE-trending Selendi basin, western Anatolia, Turkey.Turk. J. Earth Sci., 16, 117-139.

Ersoy Y., Helvacı C., Sözbilir H. (2010) - Tectono-stratigraphic evolution of the NE–SWtrending superimposed Selendi basin: implications for late Cenozoic crustal extension in Western Anatolia. Tectonophysics, 488, 210–232.

Ersoy Y., Helvacı C., Palmer M.R. (2011) - Stratigraphic, structural and geochemical features of the NE–SW trending Neogene volcano-sedimentary basins in western Anatolia: Implications for associations of supra-detachment and transtensional strike-slip basin formation in extensional tectonic setting. J. Asian Earth Sci., 41, 159–183.

Ersoy E.Y., Helvacı C., Palmer M.R. (2012) - Petrogenesis of the Neogene volcanic units in the NE-SW-trending basins in western Anatolia, Turkey. Contrib. to Mineral. Petrol., 163, 379–401.

Ersoy Y., Helvacı C., Sözbilir H., Erkül F., Bozkurt E. (2008) - A geochemical approach to Neogene–Quaternary volcanic activity of western Anatolia: an example of episodic bimodal volcanism within the Selendi Basin, Turkey. Chem. Geol., 255, 265–282.

Foley S., Musselwhite D., van der Laan, S.R. (1999) - Melt compositions from ultramafic vein assemblages in the lithospheric mantle: a comparison of cratonic and non-cratonic settings. In J. J. Gurney (Ed.), Proceedings of the 7th International Kimberlite Conference (Vol. 1, pp. 238-246). Red Roof Design.

Francis D. M. (1987) - Mantle-melt interaction recorded in spinel lherzolite xenoliths from the Alligator Lake volcanic complex, Yukon, Canada, J. Petrol., 28, 569 – 597.

Furman T. & Graham D. (1999) - Erosion of lithospheric mantle beneath the East African Rift system: evidence from the Kivu volcanic province. *Lithos,* 48, 237-262.

Furman T., Bryce J. G., Karson J. Lotti A. (2004) - East African Rift System (EARS) Plume Structure: Insights from Quaternary Mafic Lavas of Turkana, Kenya. J. Petrol., 45 (5), 1069-1088.

Georgatou A.A. & Chiaradia M. (2020) – Magmatic sulphides in high-potassium calc-alkaline to shoshonitic and alkaline rocks. Solid Earth, 11, 1-21, https://doi.org/10.5194/se-11-1-2020

Gessner, K., Markwitz, V., Güngör, T. (2018) - Crustal fluid flow in hot continental extension: tectonic framework of geothermal areas and mineral deposits in western Anatolia. Geological Society, London, Special Publications, 453 (1): 289-311. https://doi.org/10.1144/SP453.7

Gessner, K., Gallardo, L.A., Markwitz, V., Ring, U., Thomson, S.N. (2013) - What caused the denudation of the Menderes Massif: Review of crustal evolution, lithosphere structure, and dynamic topography in southwest Turkey. Gondwana Res., 24 (1), 243-274.

Gessner K., Ring U., Johnson C., Hetzel R., Passchier C. W., Güngör T. (2001) - An active bivergent rolling-hinge detachment system: Central Menderes metamorphic core complex in western Turkey. Geology, 29, 611-614.

Green D.H., Morgan J.W. Heier K. S. (1968) - Thorium, uranium and potassium abundances in peridotite inclusions and their host basalts, Earth Planet. Sci. Lett., 4, 155-166.

Grützner T., Prelevic D. Akal C. (2013) - Geochemistry and origin of ultramafic enclaves and their basanitic host rock from Kula Volcano, Turkey. Lithos 180-181, 58-73.

Güleç N. (1991) - Crust-mantle interaction in Western Turkey: implications from Sr and Nd isotope geochemistry of Tertiary and Quaternary volcanics. Geol. Mag., 128 (5), 417-435.

Haase K.M., Mühe R. Stoffers P. (2000) - Magmatism during extension of the lithosphere: geochemical constraints from lavas of the Shaban Deep, northern Red Sea. Chem. Geol., 166, 225-239.

Hakyemez H. Y., Göktaş F., & Erkal T. (2013) - Quaternary Geology and Evolution of the Gediz Graben. Geol. Bull. of Turkey, 56, 1-26.

Heineke C., Niedermann S., Hetzel R., Cüneyt Akal C. (2016) - Surface exposure dating of Holocene basalt flows and cinder cones in the Kula volcanic field (Western Turkey) using cosmogenic 3He and 10Be, Quat. Geochronol., 34, 81-91. https://doi.org/10.1016/j.quageo.2016.04.004

Helvacı C. (1995) - Stratigraphy, mineralogy, and genesis of the Bigadiç borate deposits, western Turkey. Econ. Geol., 90, 1237-1260.

Helvacı C. & Yağmurlu F. (1995) - Geological setting and economic potential of the lignite and evaporite- bearing Neogene basins of Western Anatolia, Tur- key. Isr. J. Earth Sci., Vol. 44, 91-105.

Hetzel, R., H. Zwingmann, A. Mulch, K. Gessner, C. Akal, A. Hampel, T. Güngör, R. Petschick, T. Mikes andF. Wedin (2013) - Spatiotemporal evolution of brittle normal faulting and fluid infiltration in detachment fault systems: Acase study from the Menderes Massif, western Turkey, Tectonics, 32, 364–376, https://doi.org/10.1002/tect.20031

Hofmann A.W., Jochum K.P., Seufer M., White, W.M. (1986) - Nb and Pb in oceanic basalts: new constraints on mantle evolution. Earth Planet. Sci. lett., 79, 33-45.

Holness M.B. & Bunbury, J.M. (2006) - Insights into continental rift-related magma chambers: Cognate nodules from the Kula Volcanic Province, Western Turkey. J. Volcanol. Geotherm., 153, 241-261.

Holness M.B., Cheadle M.J., Mckenzie D. (2005) - On the Use of Changes in Dihedral Angle to Decode Late-stage Textural Evolution in Cumulates. J. Petrol., 46, 8, 1565-1583.

Innocenti F., Agostini S., Di Vincenzo, G., Doglioni, C., Manetti, P., Savaşçın, M.Y. Tonarini, S. (2005) - Neogene and Quaternary volcanism in Western Anatolia: magma sources and geodynamic evolution. Mar. Geol., 221, 397-421.

Ionov D.A., Griffin W.L., O'Reilly S.O. (1997) - Volatile-bearing minerals and lithophile trace elements in the upper mantle. Chem. Geol. 141, 153–184.

Ionov D.A. & Hofmann A.W. (1995) - Nb–Ta-rich mantle amphiboles and micas: implications for subduction-related metasomatic trace element fractionations. Earth Planet. Sci. Lett., 131 (3–4), 341–356.

Işık V., Tekeli O., Seyitoğlu G. (2004) - The 40Ar/39Ar age of extensional ductile deformation and granitoid intrusions in the northern Menderes core complex: Implications for the initiation of extensional tectonics in western Turkey. J. Asian Earth Sci., 23, 555-566.

Jolivet, L., Faccenna,C.et al. (2013) - Aegean tectonics: strain localisation, slab tearing and trench retreat, Tectonophysics, 597, 1–33.

Jung S. & Masberg P. (1998) - Major-and trace-element systematics and isotope geochemistry of Cenozoic mafic volcanic rocks from the Vogelsberg (central Germany): Constraints on the origin of continental alkaline and tholeiitic basalts and their mantle sources. J. Volcanol. Geotherm., 86, 151-177.

Jung S., Vieten K., Romer R.L., Mezger K., Hoernes S., Satır M. (2012) - Petrogenesis of Tertiary Alkaline Magmas in the Siebengebirge, Germany. J. Petrol., 53 (11), 2381-2409, https://doi.org/10.1093/petrology/egs047

Karaoğlu Ö., Helvacı C., Ersoy E.Y. (2010) - Petrogenesis and 40Ar/39Ar geochronology of the volcanic rocks of the Usak–Güre basin, western Türkiye. Lithos, 119,193–210.

Khudoley A.K., Prokopiev A.V., Chamberlain K.R., Ernst R.E., Jowitt S.M., Malyshev S.V., Zaitsev A.I., Kropachev A.P. Koroleva O.V. (2012) - Early Paleozoic mafic magmatic events on the eastern margin of the Siberian Craton. Lithos, 174, 44–56.

Koçyiğit A. (2005) - The Denizli graben-horst system and the eastern limit of western Anatolian continental extension: Basin fill, structure, deformational mode, throw amount and episodic evolutionary history, SW Turkey. Geodin. Acta – Geodin. Acta. 18., 167-208. https://doi.org/10.3166/ga.18.167-208

Langmuir C.H., Vocke R.D., Hanson G.N. Hart S.R. (1978) - A general mixing equation with applications to Icelandic basalts. Earth Planet. Sci. Lett., 37, 380-392.

Le Bas, M.J., Le Maitre, R.W., Streckeisen, A. Zanetti, B. (1986) - A chemical classification of volcanic rock based on the total alkali - silica diagram. J. Petrol., 27, 745-750.

Leake B.E., Woolley A.R., Arps C.E.S., Birch W.D., Gilbert M.C., Grice, J.D., Hawthorne, F.C., Kato A., Kisch H.J., Krivovichev VG., Linthout K., Laird J., Mandarino J., Maresch, W.V., Nickel, E.H., Rock N.M.S. Schumacher J.C., Smith D.C., Stephenson N.C.N., Ungaretti L., Whittacker E.J.W., Youzhi G. (1997) - Nomenclature of amphiboles; Report of the Subcommittee on Amphiboles of the International Mineralogical Association Commission on New Minerals and Mineral Names, Eur. J. Mineral., 9, 623-651.

Lips A., Cassard D. Sözbilir H., Yılmaz H. Wijbrans J.R. (2001) - Multistage exhumation of the Menderes Massif, Western Anatolia (Turkey). Int. J. Earth Sci., 89. 781-792. https://doi.org/10.1007/s005310000101

Maddy, D., Schreve, D., Demir, T., Veldkamp, A., Wijbrans, J.R., van Gorp, W., van Hinsbergen, D.J.J., Dekkers, M.J., Scaife, R., Schoorl, J.M., Stemerdink, C., van der Schriek, T., (2015) - The earliest securely-dated hominin artefact in Anatolia?, Quat. Sci. Rev., 109, 68-75. https://doi.org/10.1016/j.quascirev.2014.11.021

Mahatsente R., Alemdar S., Çemen I. (2017) - "Effect of slab-tear on crustal structure in Southwestern Anatolia: insight from gravity data modeling," in Neotectonics and Earthquake Potential of the Eastern Mediterranean Region, Geophysical Monograph Series, American Geophysical Union.

Mayer B., Jung S., Romer R.L., Stracke A., Haase K.M., Garbe-Schönberg, C.D. (2013) Petrogenesis of Tertiary hornblende–bearing lavas in the Rhön, Germany, J. Petro., 54, 2095-2123. https://doi.org/10.1016/j.lithos.2021.106431

McDonough W.F. (1990) - Constraints on the composition of the continental lithospheric mantle. Earth Planet. Sci. Lett., 101, 1-18.

McKenzie D. (2020) - The structure of the lithosphere and upper mantle beneath the Eastern Mediterranean and Middle East. Med. Geosc. Rev., 2, 311–326. https://doi.org/10.1007/s42990-020-00038-1

McKenzie D.P. & O'Nions R.K. (1991) - Partial melt distributions from inversion of rare earth element concentrations. J. Petrol., 32, 1021-1091.

Meng F., Gao S., Niu Y., Liu Y. Wang X. (2015) - Mesozoic–Cenozoic mantle evolution beneath the North China Craton: A new perspective from Hf–Nd isotopes of basalts. Gondwana Res., 27,4, 1574-1585. https://doi.org/10.1016/j.gr.2014.01.014

Miyashiro A. (1978) - Nature of alkalic volcanic rock series. Contrib. Mineral. Petrol., 66, 91-104.

Mollo S., Giacomoni P.P., Coltorti M., Ferlito C., Lezzi G., Scarlato P. (2015) - Reconstruction of magmatic variables governing recent Etnean eruptions: constraints from mineral chemistry and P–T–fO_2–H_2O modeling. Lithos, 212–215, 311–320.

Morimoto N., Fabries J., Ferguson A., Ginzburg I., Roos M., Seifert F., Zussman J. (1988) - Nomenclature of pyroxenes, Bull. Mineral., 111, 535-550.

Moufti M.R., Moghazi A.M., Ali K.A. (2012) - Geochemistry and Sr–Nd–Pb isotopic composition of the Harrat Al-Madinah Volcanic Field, Saudi Arabia, *Gondwana Res.,* 21, 670-689.

Nakamura N. (1974) - Determination of REE, Ba, Fe, Mg, Na and K in carbonaceous and ordinary chondrites. Geochim. Cosmochim. Acta, 38, 757-775.

Neave D. & Putirka K. (2017) - A new clinopyroxene-liquid barometer, and implications for magma storage pressures under Icelandic rift zones. Am. Min., 102: 777-794.

Nikogosian I.K., Bracco Gartner A.J.J., van Bergen M.J., Mason P.R.D., van Hinsbergen, D.J.J. (2018) - Mantle sources of recent Anatolian intraplate magmatism: A regional plume or local tectonic origin? Tectonics, 37, 4535–4566. https://doi.org/10.1029/2018TC005219

Okay A.I., Zattin M, Cavazza W (2010) - Apatite fission-track data for Miocene Arabia-Eurasia collision. Geology 38: 35-38

Pasquaré G., Poli S., Vezzoli L., Zanchi A. (1988) - Continental Arc Volcanism and Tectonic Setting In Central Anatolia, Turkey. Tectonophysics, 146, 1-4, 217-230.

Pearce J.A. & Cann J.R. (1973) - Tectonic setting of basic volcanic rocks determined using trace element analysis. Earth Planet. Sci. Lett., 19, 290-300.

Pearce J.A. (1983) - The role of subcontinental lithosphere in magma genesis at active continental margins. In: Continental basalt and Mantle xenolits, C. J. Hawkesworth and M.J. Nory (eds) 230-249.

Pilet S., Baker, M.B., Stolper, E.M. (2008). Metasomatized lithosphere and the origin of alkaline lavas. Science, 320, 916-919.

Pilet S., Ulmer P., Villiger, S. (2010) - Liquid line of descent of a basanitic liquid at 1·5 GPa: constraints on the formation of metasomatic veins. Contrib. to Mineral. Petrol., 159, 621-643.

Polo L.A., Giordano D., Janasi V.A., Guimaraes L.F. (2017) - Effusive silicic volcanism in Parana Magmatic Province, South Brazil: Physico-chemical conditions of storage and eruption and considerations on the rheological behavior during emplacement. J. Volcanol. Geotherm., 355, 115-135. https://dx.doi.org/10.1016/j.jvolgeores.2017.05.027

Prelevic D., Akal C., Foley S.F., Romer R.L., Stracke A., Van Den Bogaard P. (2012) - Ultrapotassic mafic rocks as geochemical proxies for post-collisional Dynamics of orogenic lithospheric mantle: the case of southwestern Anatolia, Turkey. J. Petrol., 53 (5), 1019–1055. https://doi.org/10.1093/petrology/egs008

Putirka K.D. (1999) - Clinopyroxene+liquid equilibrium to 100 kbar and 2450 K. Contrib. to Mineral. Petrol., 135, 151-163.

Putirka K.D. (2008) - Thermometers and barometers for volcanic systems. In: Putirka K, Tepley F (eds) Minerals, Inclusions and Volcanic Processes, Reviews in Mineralogy and Geochemistry, MSA, 69, 61-120.

Putirka K., Johnson M., Kinzler R., Longhi J., Walker D. (1996) - Thermobarometry of mafic igneous rocks based on clinopyroxene-liquid equilibria, 0-30 kbar. Contrib. to Mineral. Petrol., 123, 92-108.

Purvis M. & Robertson A.H.F. (2004) - Neogene crustal extension in western (Aegean) Turkey: evidence from the Alaşehir graben and the Selendi and Gördes basins. Tectonophysics 391, 171–201.

Ring U. & Layer P. (2003) - High-pressure metamorphism in the Aegean, eastern Mediterranean: Underplating and exhumation from the Late Cretaceous until the Miocene to Recent above the retreating Hellenic subduction zone. Tectonics, 22, 3, 6(1-23). https://doi.org/10.1029/2001TC001350

Rieder M., Cavazzini G., D'Yakonov Yu.S., Frank-Kamenetskii V.A., Gottardi G., Guggenheim S., Koval P.V., Müller G., Neiva A.M.R., Radoslovich E.W., Robert J.-L.,

Sassi F.P., Takeda H., Weiss Z., Wones D.R. (1998) - International Mineralogical Association Report: Nomenclature of the micas, Mineral. Mag., 63, 267-279.

Rojay B., Toprak V., Demirci C., Süzen, M. (2005) - Plio-Quaternary evolution of the Küçük Menderes Graben Southwestern Anatolia, Turkey. Geodin. Acta., 18, 317-331. 10.3166/ga.18.317-331.

Rollinson H.R. (1993) - Using geochemical data: evaluation, presentation, interpretation. Longman Scientific and Technical, John Wiley and Sons, Inc., New York, 352p.

Salaün G., Pedersen H.A., Paul A., Farra V., Karabulut H., Hatzfeld D., Papazachos C., Childs D.M., Pequegnat C., SIMBAAD Team (2012) - High-resolution surface wave tomography of the Aegean-Anatolia region: constraints on upper mantle structure, Geophys. J. Int., 190, 406–420. https://doi.org/10.1111/j.1365-246X.2012.05483.x

Saunders P., Priestley K., Taymaz T. (1998) - Variations in the crustal structure beneath western Turkey. Geophys. J. Int., 134, 373–389.

Seyitoğlu G. & Scott B.C. (1991) - Late Cenozoic crustal extension and basin formation in west Turkey. Geol. Mag., 128, 155-166.

Seyitoğlu G. & Scott B.C. (1992) - Late Cenozoic volcanic evolution of the NE Aegean region. J. Volcanol. Geotherm., 54, 157-176.

Seyitoğlu G. & Scott B. C. (1994) - Late Cenozoic basin development in west Turkey. Gordes basin: tectonics and sedimentation. Geol. Mag., 131, 631-637.

Seyitoğlu G. & Scott B.C. (1996) - The cause of N-S extensional tectonics in western Turkey: Tectonic escape vs Back-arc spreading vs Orogenic collapse. J. Geodyn., 22, 145-153.

Seyitoğlu G. (1997) - Late Cenozoic tectono-sedimentary development of Selendi and Uşak-Güre basins: a contribution to the discussion on the development of east-west and north-trending basins in western Turkey. Geol. Mag., 134, 163-175.

Seyitoğlu G., Tekeli O., Çemen İ., Şen S., Işık V. (2002) - The role of the flexural rotation/rolling hinge model in the tectonic evolution of the Alaşehir graben, western Turkey. Geol. Mag., 139, 15–26.

Seyitoğlu G., Aktuğ B., Esat K., Kaypak B. (2022) - Neotectonics of Turkey (Türkiye) and surrounding regions: a new perspective with block modelling. Geol. Acta, 20.4, 1-21. https://doi.org/10.1344/GeologicaActa2022.20.4

Shaw D.M. (1970) - Trace element fractionation during anatexis. Geochim. Cosmochim. Acta, 34, 237-243.

Shaw J.E., Baker J.A., Menzies M.A., Thirlwall M.F., Ibrahim K.M. (2003) - Petrogenesis of the Largest Intraplate Volcanic Field on the Arabian Plate (Jordan): a Mixed Lithosphere–Asthenosphere Source Activated by Lithospheric Extension. J. Petrol., 44 (9): 1657-1679.

Sözbilir H. (2002) - Geometry and origin of folding in the Neogene sediments of the Gediz Graben, western Anatolia, Turkey. Geodin. Acta, 15, 277-288.

Sözbilir H. (2005) - Oligo-Miocene extension in the Lycian orogen: evidence from the Lycian molasse basin, SW Turkey, Geodin. Acta, 18:3-4, 255-282. https://doi.org/10.3166/ga.18.255-282

Sölpüker U. (2007) - Petrology of Kula Volcanic Province, Western Turkey. Dissertation University of Cincinnati (Available online at http://etd.ohiolink.edu/view.cgi?acc_num=ucin1187013478).

Spera F. J. (1984) - Carbon dioxide in petrogenesis III: role of volatiles in the ascent of alkaline magma with special reference to xenolith-bearing mafic lavas. Contrib. Miner. Petrol., 88, 217–232.

Streckeisen A. (1976) - To each plutonic rock its proper name. Earth Sci. Rev., 12, 1-33.

Sun P., Niu Y., Guo P., Cui H., Ye L. and Liu J. (2018) – The evolution and ascent paths of mantle xenolith-bearing magma: Observations and insights from Cenozoic basalts in Southeast China. Lithos, 310–311, 171–181. https://doi.org/10.1016/j.lithos.2018.04.015

Şengör A.M.C. (1979) - The North Anatolian transform fault: its age, offset and tectonic significance. J. Geol. Soc., 136, 269-282.

Şengör A.M.C. & Yılmaz, Y. (1981) - Tethyan evolution of Turkey: a plate tectonic approach. Tectonophysics, 75, 181-241.

Şengör A.M.C. & Yazıcı M. (2020) - The aetiology of the neotectonic evolution of Turkey. Med. Geosc. Rev., 2, 327–339. https://doi.org/10.1007/s42990-020-00039-0

Tang Y.J., Zhang H.F., Ying J.F. (2006) - Asthenosphere–lithospheric mantle interaction in an extensional regime: Implication from the geochemistry of Cenozoic basalts from Taihang Mountains, North China Craton. Chem. Geol., 233, 309-327.

Thompson R.N. (1982) - Magmatism of the British Tertiary province. Scott. J. Geol., 18, 49-107

Tokçaer M., Agostini S., Savaşçın M.Y. (2005) - Geotectonic setting and origin of the youngest Kula volcanics (Western Anatolia), with a new emplacement model. Turk. J. Earth Sci. 14, 145–166.

Tschegg C., Ntaflos, T., Akinin V. (2011) - Polybaric petrogenesis of Neogene alkaline magmas in an extensional tectonic environment: Viliga Volcanic Field, northeast Russia. Lithos, 122, 13-24.

Ulusoy İ., Sarıkaya M.A., Schmitt A.K., Şen E., Danišík M., Gümüş E. (2019) - Volcanic eruption eye-witnessed and recorded by prehistoric humans, Quat. Sci. Rev., 212, 187-198. https://doi.org/10.1016/j.quascirev.2019.03.030.

Wang K., Plank T., Walker J. D., Smith E. I. (2002) - A mantle melting profile across the Basin and Range, SW USA. J. Geophys. Res. 107 (10), 1029-2001. https://doi.org/10.1029/2001JB000209

Wang K.L., Chung S.L., O'Reilly S., Sun S.S., Shinjo R., Chen C.H. (2004) - Geochemical Constraints for the Genesis of Post-Collisional Magmatism and the Geodynamic Evolution of the Northern Taiwan Region. J. Petrol., 45 (5), 975-1011.

Watson B.E. (1980) - Apatite and phosphorus in mantle source regions: an experimental study of apatite/melt equilibria at pressures to 25 kbar. Earth Planet. Sci. Lett., 51, 322-335.

Westaway R., Pringle M., Yurtmen S., Demir T., Bridgland D., Rowbotham G., Maddy D. (2004) - Pliocene and Quaternary regional uplift in western Turkey: The Gediz river terrace staircase and the volcanism at Kula. Tectonophysics, 391, 121–169

Westaway R., Guillou H., Yurtmen S., Demir T., Scaillet S., Rowbotham G. (2005) - Constraints on the timing and regional conditions at the start of the present phase of crustal extension in western Turkey, from observations in and around the Denizli region. Geodin. Acta, 18, 209-238.

Westaway R., Guillou H., Yurtmen S., Beck A., Bridgland D., Demir T., Scaillet, S., Rowbotham G. (2006) - Late Cenozoic uplift of western Turkey: Improved dating of the Kula Quaternary volcanic field and numerical modelling of the Gediz river terrace staircase. Glob. Planet. Change, 51, 131–171

Whitney, D.L. & Evans, B.W. (2010) - Abbreviations for Names of Rock-Forming Minerals. American Mineralogist, 95, 185-187. http://dx.doi.org/10.2138/am.2010.3371

Wilson M. (1989) - Igneous petrogenesis, Unwin Hyman, London, 466p.

Worthing M.A. & Nasir S. (2008) - Cambro-Ordovician potassic (alkaline) magmatism in Central Oman: Petrological and geochemical constraints on petrogenesis. Lithos, 106, 25-38.

Yaxley G. M., Crawford A.J., Green D.H. (1991) - Evidence for carbonatite metasomatism in spinel peridotite xenoliths from western Victoria, Australia. Earth Planet. Sci. Lett., 107, 305-317.

Yaxley G.M., Kamenetsky V.S., Green D.H., Falloon T.J. (1997) - Glasses in mantle xenoliths from western Victoria, Australia, and their relevance to mantle processes, Earth. Plan. Sci. Lett., 148, 433-446.

Yılmaz Y; Şaroğlu F; Güner Y. (1987) - Initiaton of the Neomagmatism in East Anatolia. Tectonophysics, 134, 1-3, 177-199.

Yılmaz Y. (1989) - An approach to the origin of young volcanic rocks of western Turkey. Tectonic Evolution of the Tethyan Region (Ed: A.M.C. Şengör), Kluwer Academic Publishers, Dordrecht, 159-189.

Yılmaz Y. (1990) - Comparison of young volcanic associations of western and eastern Anatolia formed under a compressional regime: a review. J. Volcanol. Geotherm., 44, 69-77.

Yılmaz Y., Genç S.C., Gürer O.F., Bozcu M., Yılmaz K. (2000) - When did the Western Anatolian grabens begin to develop? In: Bozkurt E, Winchester JA, Piper JDA (editors), Tectonics and Magmatism in Turkey and the Surrounding Area. Geol. Soc. Special Publication, London 173: 353-384.

Zhu L., Mitchell B.J., Akyol N., Cemen I., Kekovalı K. (2006) - Crustal thickness variations in the Aegean region and implications for the extension of continental crust, J. Geophys. Res. Sol. Earth, 1978–2012, 111(B1). https://doi.org/10.1029/2005JB003770

FIGURE CAPTIONS

Figure 1. a) Geodynamical sketch map of Anatolian block, locations of major faults and study area shown on Digital Elevation Model (DEM) of Anatolia. (AEZ: Aegean Extension Zone; NAF: North Anatolian Fault; EAF: East Anatolian Fault; EF: Ecemiş Fault; TGF: Tuz Gölü Fault and OF: Ovacık Fault. Big arrows indicate the sense of plate motion and half arrows show the relative motion direction on the faults). b) Map showing hillshade topography of the western Anatolia. Faults and graben boundaries are taken from Karaoğlu et al. (2010) and Ersoy et al. (2011, 2012). The pale yellow-coloured dashed line refers to the Menderes Massif (Gessner et al., 2018). GG: Gediz graben, SG: Simav graben, KmG: Küçük Menderes graben, BmG: Büyük Menderes graben, GöB: Gördes basin, DB: Demirci basin, SB: Selendi basin, GüB: Güre basin, NMM: Northern Menderes Massif, CMCC: Central Menderes Core Complex, ÇS: Çine Submassif.

Figure 2. Geological map of the Kula Volcanic Field (modified from Ercan et al., 1978) and published age data. [1]: Westaway et al., 2006, [2]: Westaway et al., 2004, [3]: Maddy et al., 2015, [4]: Bunbury, 2001, [5]: Heineke et al., 2016, [6]: Ulusoy et al., 2019 (Age data is only for Çakallar Divlit Tepe cone and lava flows near Demirköprü Dam). M1-3: tuff ring, M4: maar, Gm: groundmass, Amp: amphibole, ZDD: Zircon double-dating, Cosm: cosmogenic. Geological map draped over SRTM 1 Arc-Second Global DEM hillshade (EROS, 2018); Coord. Sys: UTM, datum: ED1950.

Figure 3. Field photographs: a) Base surge deposits of Kızıl Tepe tuff ring (M3). Olivine bearing ultramafic enclaves are dominant in lithic-rich layers. Hammer is 30 cm long. b) Small cinder cones having basal diameter and height of 100-150 m and 20-30 m, respectively (northern side of Divlit Tepe near Kula). c) Bağ Tepe, a breached cinder cone, with lava extrusions ceased its activity. It is rich in hornblendite (hammer is 30 cm long). d) Enclaves marked by red arrows in M3 tuff ring deposits (BII) varying in size

from <3 to 16 cm, inset images; macro and thin section view. e) and f) Rounded and sub-rounded hornblendite enclaves (marked by red arrows) in the lava flow erupted from Bağ Tepe cinder cone (BIII). Hammer is 30 cm long, inset image; broken sample. g) Wehrlite sample (K97-10a2, BII) from M3 tuff ring. Notice the broken and unbroken vesicles. Inset image; macro view. Cpx: clinopyroxene, Ol: olivine, Phl: phlogopite.

Figure 4. Photomicrographs of the host rock in the KVF (plane-polarized). a) Skeletal olivine phenocryst. Groundmass; microphenocryst to fine microlite and microcryst (BI). b) Olivine phenocryst and euhedral spinel inclusions (BIII). c) Sub-rounded olivine, fresh hornblende phenocrysts and leucites in the groundmass (BII). d) Hornblende and euhedral spinel microphenocrysts (BIII). e) Green-coloured, relict clinopyroxene core is mantled by another clinopyroxene showing a distinct pleochroism. Note the glass inclusions at the reaction zone (BII). Micro-enclaves containing quenched interstitial glass: (f) hornblendite (BIII), (g) Phl-Cpx-hornblendite (BIII) and (h) clinopyroxenite (BII). Ol: olivine, Cpx: clinopyroxene, Hbl: hornblende, Pl: plagioclase, Lct: leucite, Nph: nepheline, Spl: spinel, G: glass and V: vesicle.

Figure 5. Classification of the enclaves according to their modal mineralogy (Streckeisen, 1976).

Figure 6. Photomicrographs of the enclaves containing glass (G) and vesicle (V), plane-polarized: a) Hornblendite (BII); prismatic hornblende (Hbl) aggregates in very pale brown coloured vesicular glass. b) Hornblendite (BIII); euhedral hornblende and clinopyroxene (Cpx) in brown coloured vesicular glass. Apatite (Ap) is not only observed as inclusion in Hbl and Cpx, but also in the glass. c) Same sample as (b). Note some apatites showing an elongation from towards the glass. d) Cpx-hornblendite (BII); euhedral and embayed hauyne (Hyn) containing glass inclusions. Some are clear and embayed. The colour of the glass is changing from dark brown to light brown. It is darker in colour towards to

hornblende and clinopyroxene in contrast to hauyne crystal. e) Pl-bearing Phl-Cpx-hornblendite (BII); plagioclase (Pl) showing sieve texture. It is enclosing euhedral apatite crystals. Note the clinopyroxene microcryst in the glass (arrowed), lining up around the hornblende crystals. f) Phl-clinopyroxenite (BIII); clinopyroxene and embayed phlogopite (Phl) crystals. Detached phlogopite pieces and main crystal show optically continuity. Note the clinopyroxene microcrysts in the black coloured glass. g) Wehrlite (BII); clinopyroxene, embayed olivines with inclusion of spinel (Spl) and embayed hornblende crystals in a Gp. Hornblende has ragged edge formed by partial melting. h) Wehrlite (BII); poikilitic hornblende enclosing olivine and clinopyroxene. Note the curved marks inside the hornblende, (BII). i) Hornblendite (BIII); oriented long prismatic hornblendes with Gim (interstitial vesicular glass). j) Hbl-clinopyroxenite (BII); inter-granular dark coloured Gp (glass pockets). k) Ol-Hbl-clinopyroxenite (BII); replacements of clinopyroxene by hornblende along cleavage planes and alteration of olivine to iddingsite along rims and cracks. l) Hbl-gabbro (BIII); dusty rimmed plagioclase enclosing clinopyroxenes and apatite. m) Hbl-gabbro (BIII); fine-grained phlogopites formed around the relict olivine. n) Wehrlite (BII); glass associated with inter-granular minerals of sub-hedral olivines, clinopyroxenes and hornblendes.

Figure 7. Composition of clinopyroxenes from host rock and enclaves plotted in the ternary system Wo-En-Fs, with fields from Morimoto et al. (1988).

Figure 8. Total Alkali Silica classification diagram (Le Bas et al., 1986) for the host rock and glass in enclaves. The dashed line separates alkali and subalkaline fields, after Miyashiro (1978). Small circle symbols of host rocks are from Alıcı et al. (2002). Phl: phlogopite, Cpx: clinopyroxene, Hbl: hornblende

Figure 9. Major (wt.%) and trace (ppm) element abundances versus SiO_2 for host rock and enclaves.

Figure 10. a) and b) MORB-normalised (Pearce, 1983) incompatible trace element patterns of host rocks and enclaves. c) and d) Chondrite-normalised (Nakamura, 1974) REE patterns of host rocks and enclaves.

Figure 11. a) Ba/Rb versus Rb/Sr diagram (Furman & Graham 1999) of host rocks and enclaves. SCLM: Sub-continental lithospheric mantle. b) and c) Sm/Yb – La/Yb and (Tb/Yb)n – (La/Yb)n non-modal batch melting (Shaw, 1970) diagrams showing the melt curves of spinel ($Ol_{0.62/-0.40}$ +$Opx_{0.24/0.30}$ +$Cpx_{0.12/0.90}$ +$Spinel_{0.02/0.20}$) and garnet-peridotite ($Ol_{0.66/0.1}$+ $Opx_{0.27/0.18}$ +$Cpx_{0.03/0.3}$ +$garnet_{0.04/0.42}$) and binary mixing line between spinel and garnet peridotite melting curves. Normalisation values are from Thompson (1982). The horizontal black dashed line separates the melting fields of garnet and spinel-peridotite (Wang et al., 2002). d) Yb-La/Yb diagram showing spinel and garnet non-modal batch melting curves. Initial concentrations for La, Sm, Yb and Tb are from McDonough (1990). Subscripts of spinel and garnet-peridotite mineral compositions refer source mode/melts modes during non-modal batch melting. Source and melt modes of spinel and garnet peridotites are from McDonough (1990) and Wang et al. (2004), respectively. Partial melting coefficients are compiled from McKenzie & O'Nions (1991); Rollinson (1993) and Elkins et al. (2008).

Figure 12. Pressure-temperature diagram illustrating the potential source region for host rocks and enclaves from the KVF (adopted from Jung et al., 2012 and references therein). Cpx pressure and temperature estimates based on Neave & Putirka (2017) and Putirka (2008; eqn. 33), respectively. The average Moho depth is accepted as ~30 km from Saunders et al. (1998), Zhu et al. (2006), Mahatsente et al. (2017) and Artemieva & Shulgin (2019).

Figure 13. Schematic illustration showing the evolution and probable conduits of the Kula volcanism prior to eruption. The depth of lithosphere-asthenosphere boundary (LAB) is

accepted as ca. 80 km from Salaün et al. (2012), Mahatsente et al. (2017) and Artemieva & Shulgin (2019). However, it is thought that the depth of the LAB decreases from 80 km in the northwest and 105 km in the southeast (brown-coloured arrows) to ca. 60 km beneath the Kula volcanic field (i.e. Artemieva & Shulgin, 2019) based on calculated P-T values. The depth of the lens-shaped magma chambers including ultramafic cumulates resulting from fractional crystallisation (FC) is calculated using the Cpx-melt thermobarometers.

TABLE CAPTIONS

Supplementary Table 1. Modal mineralogy of the glass bearing enclaves.

Supplementary Table 2. Selected microprobe analyses of olivines from the host rocks and enclaves.

Supplementary Table 3. Selected microprobe analyses of clinopyroxenes from the host rocks and enclaves. Nomenclature after Morimoto et al. (1988).

Supplementary Table 4. Selected microprobe analyses of hornblendes from the host rocks and enclaves. Nomenclature after Leake et al. (1997).

Supplementary Table 5. Representative microprobe analyses of phlogopites.

Supplementary Table 6. Selected microprobe analyses of plagioclases.

Supplementary Table 7. Selected microprobe analyses of feldspathoids.

Supplementary Table 8. Microprobe analyses of oxides.

Supplementary Table 9. Microprobe analyses of the glasses from enclaves.

Supplementary Table 10. Major and trace-element analyses for the KVF.

Supplementary Table 11. Minimum and maximum T-P values from the clinopyroxene thermometer of Neave & Putirka (2007) and Putirka (2008, eqn. 33). Cpx-liquid test between the predicted and observed Diopside-Hedenbergite (DiHd) components, calculated by Putirka et al. (1996) and Putirka (1999). Blue lines are the equilibrium range accepted as 10% deviation to one-to-one line.

Supplementary Data 1. T-P calculation Excel spreadsheet.

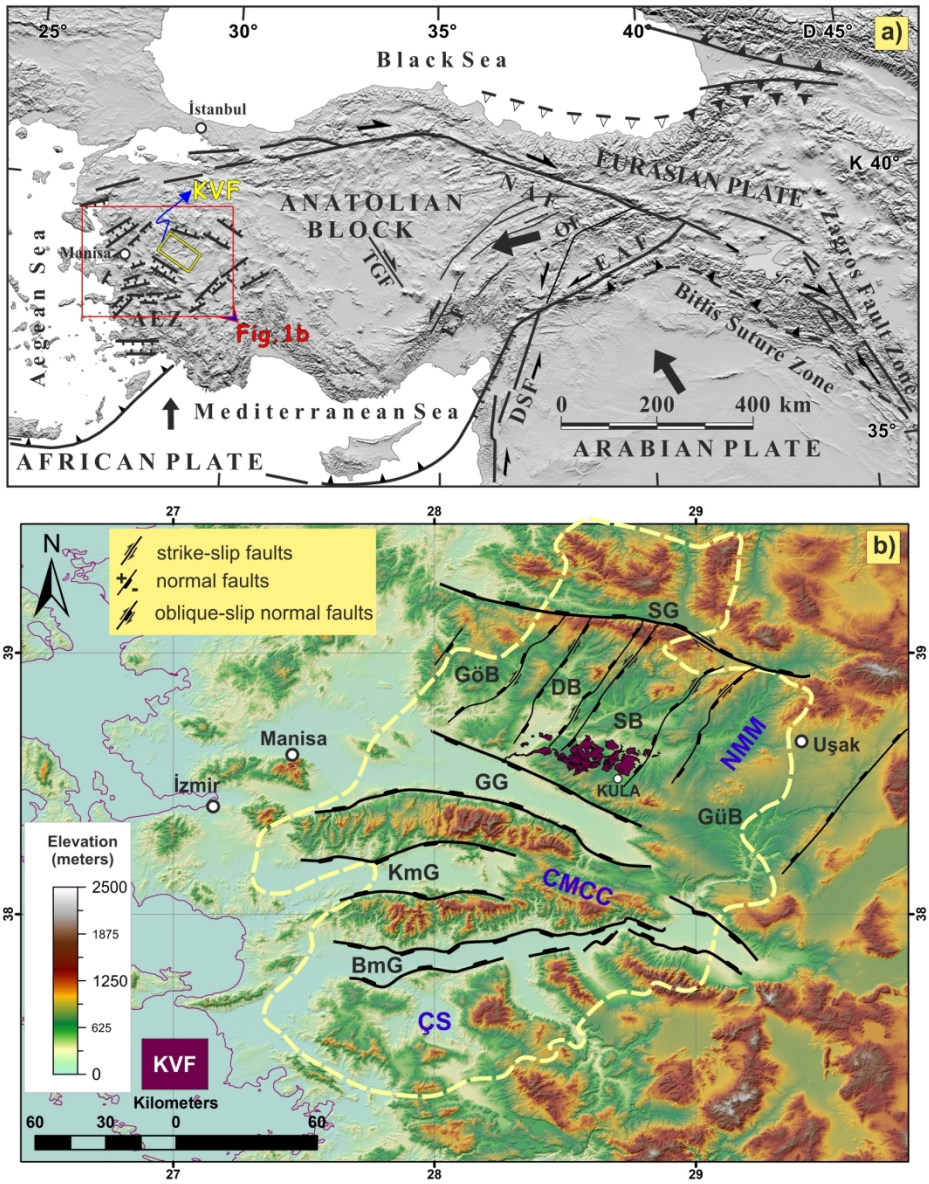

Figure 1

163x208mm (300 x 300 DPI)

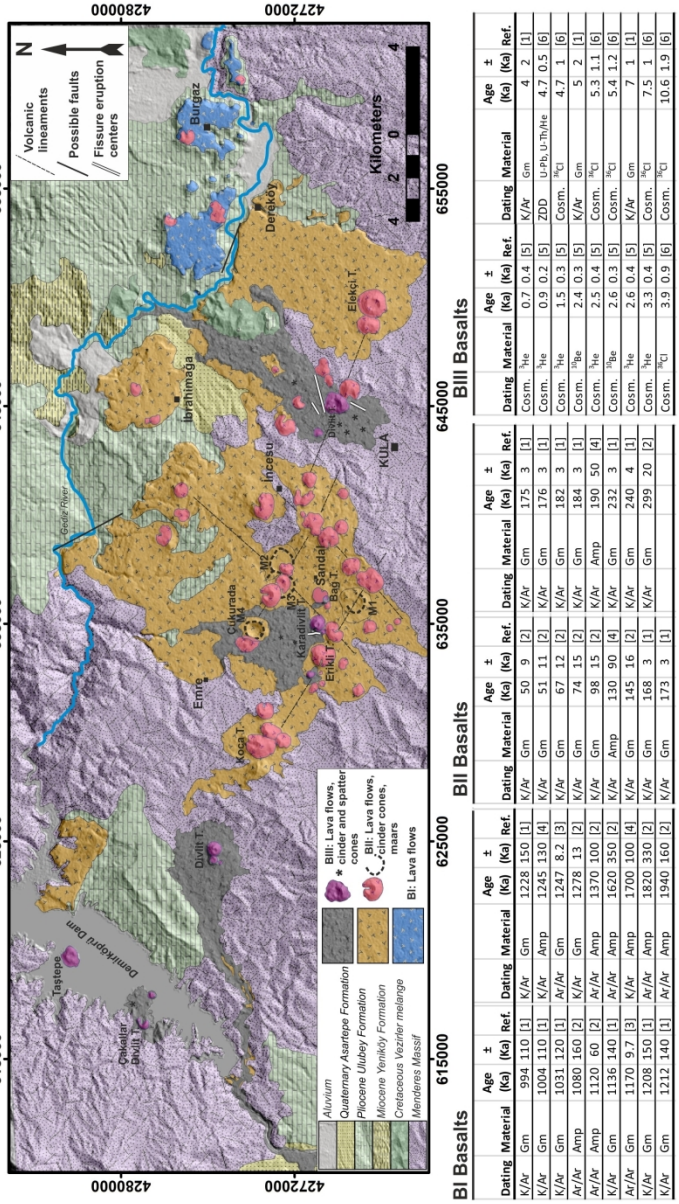

BI Basalts

Dating	Material	Age (Ka)	± (Ka)	Ref.
K/Ar	Gm	994	110	[1]
K/Ar	Gm	1004	110	[1]
K/Ar	Gm	1031	120	[1]
Ar/Ar	Amp	1080	160	[2]
Ar/Ar	Amp	1120	60	[2]
K/Ar	Gm	1136	140	[1]
Ar/Ar	Gm	1170	9.7	[3]
K/Ar	Gm	1208	150	[1]
K/Ar	Gm	1212	140	[1]
Ar/Ar	Amp	1228	150	[1]
K/Ar	Amp	1245	130	[4]
Ar/Ar	Gm	1247	8.2	[3]
K/Ar	Gm	1278	13	[2]
Ar/Ar	Amp	1370	100	[2]
Ar/Ar	Amp	1620	350	[2]
K/Ar	Amp	1700	100	[4]
Ar/Ar	Amp	1820	330	[2]
Ar/Ar	Amp	1940	160	[2]

BII Basalts

Dating	Material	Age (Ka)	± (Ka)	Ref.
K/Ar	Gm	50	9	[2]
K/Ar	Gm	51	11	[2]
K/Ar	Gm	67	12	[2]
K/Ar	Gm	74	15	[2]
K/Ar	Gm	98	15	[2]
K/Ar	Amp	130	90	[4]
K/Ar	Gm	145	16	[2]
K/Ar	Gm	168	3	[1]
K/Ar	Gm	173	3	[1]
K/Ar	Gm	175	3	[1]
K/Ar	Gm	176	3	[1]
K/Ar	Gm	182	3	[1]
K/Ar	Gm	184	3	[1]
K/Ar	Amp	190	50	[4]
K/Ar	Gm	232	3	[1]
K/Ar	Gm	240	4	[1]
K/Ar	Gm	299	20	[2]

BIII Basalts

Dating	Material	Age (Ka)	± (Ka)	Ref.
Cosm.	^{3}He	0.7	0.4	[5]
Cosm.	^{3}He	0.9	0.2	[5]
Cosm.	^{3}He	1.5	0.3	[5]
Cosm.	^{10}Be	2.4	0.3	[5]
Cosm.	^{3}He	2.5	0.4	[5]
Cosm.	^{10}Be	2.6	0.3	[5]
Cosm.	^{3}He	2.6	0.4	[5]
Cosm.	^{3}He	3.3	0.4	[5]
Cosm.	^{36}Cl	3.9	0.9	[6]
K/Ar	Gm	4	2	[1]
ZDD	U-Pb, U-Th/He	4.7	0.5	[6]
Cosm.	^{36}Cl	4.7	1	[6]
K/Ar	Gm	5	2	[1]
Cosm.	^{36}Cl	5.3	1.1	[6]
Cosm.	^{36}Cl	5.4	1.2	[6]
K/Ar	Gm	7	1	[1]
Cosm.	^{36}Cl	7.5	1	[6]
Cosm.	^{36}Cl	10.6	1.9	[6]

Figure 2

158x272mm (300 x 300 DPI)

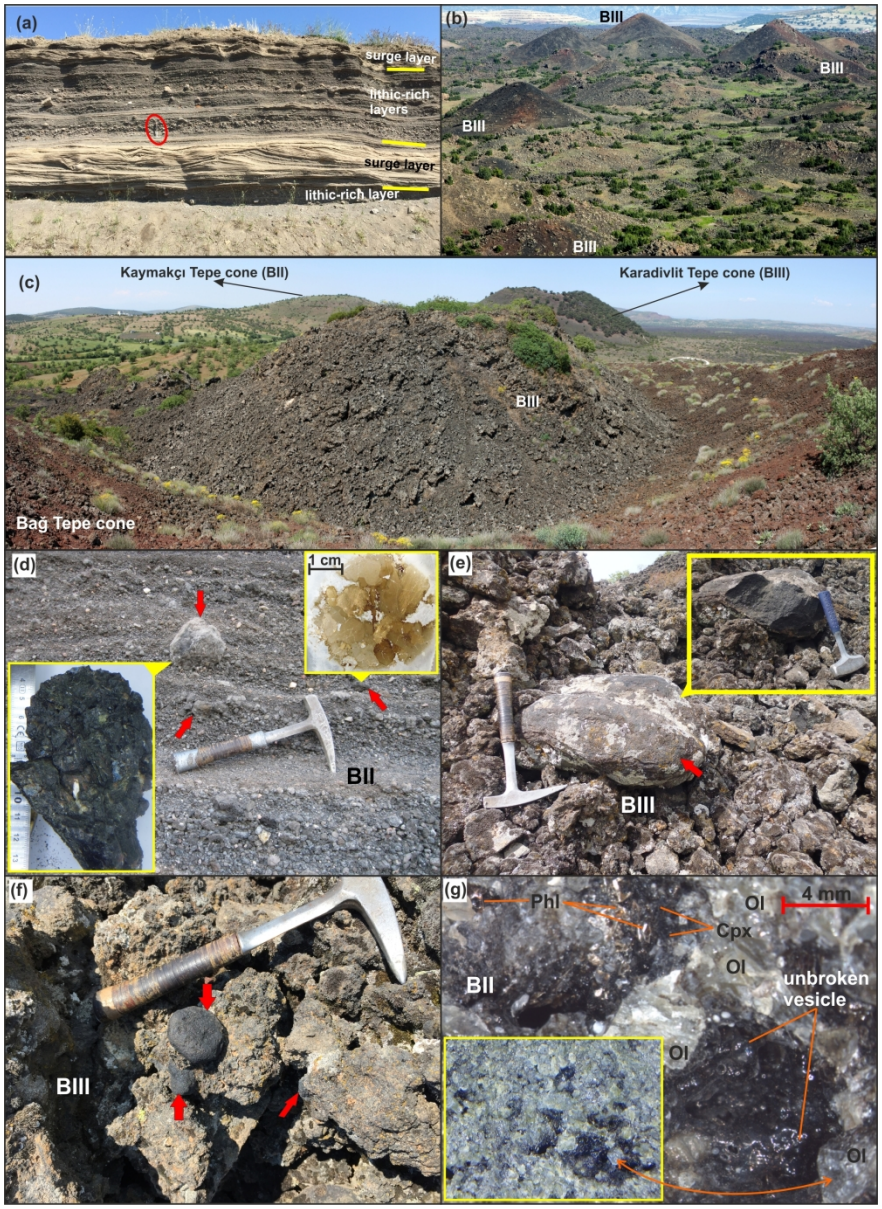

Figure 3

195x268mm (300 x 300 DPI)

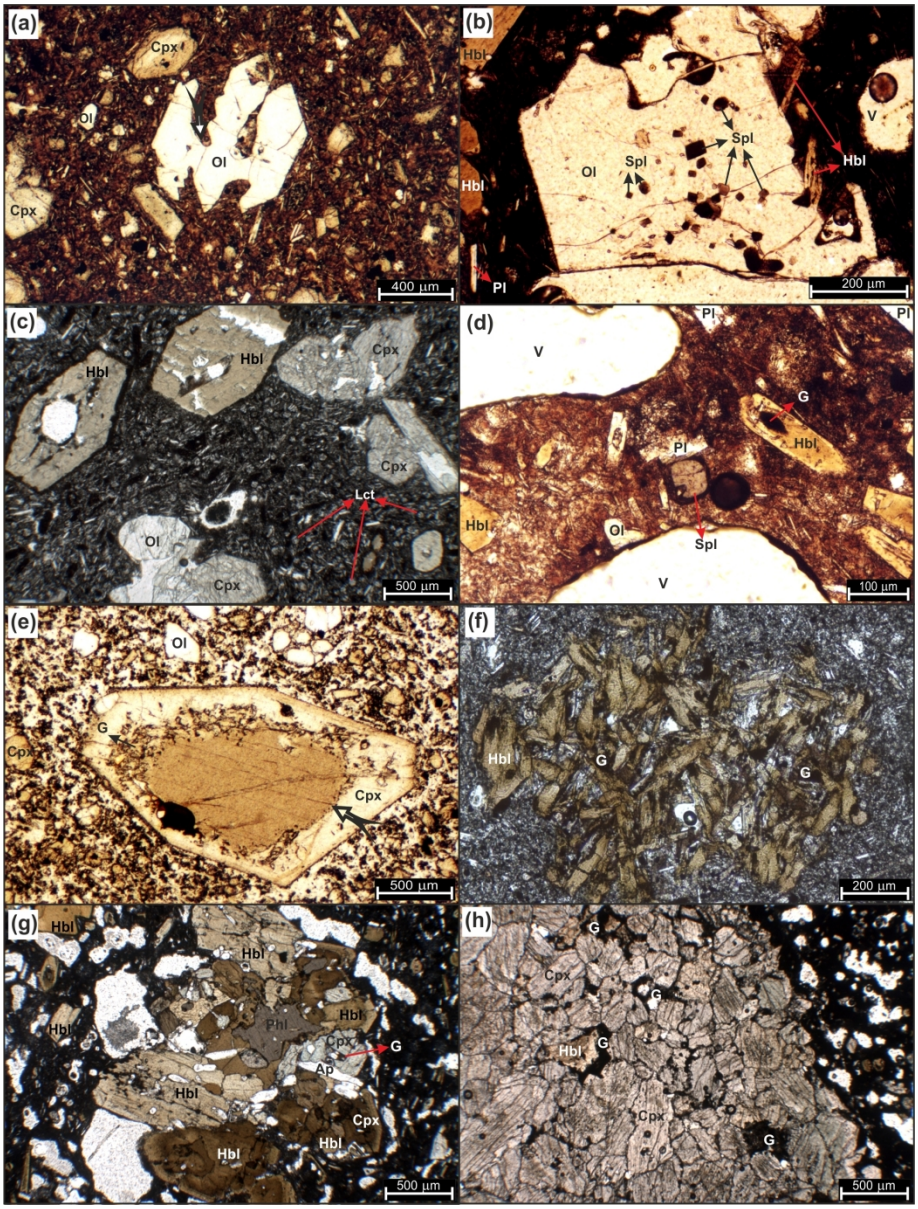

Figure 4

182x240mm (300 x 300 DPI)

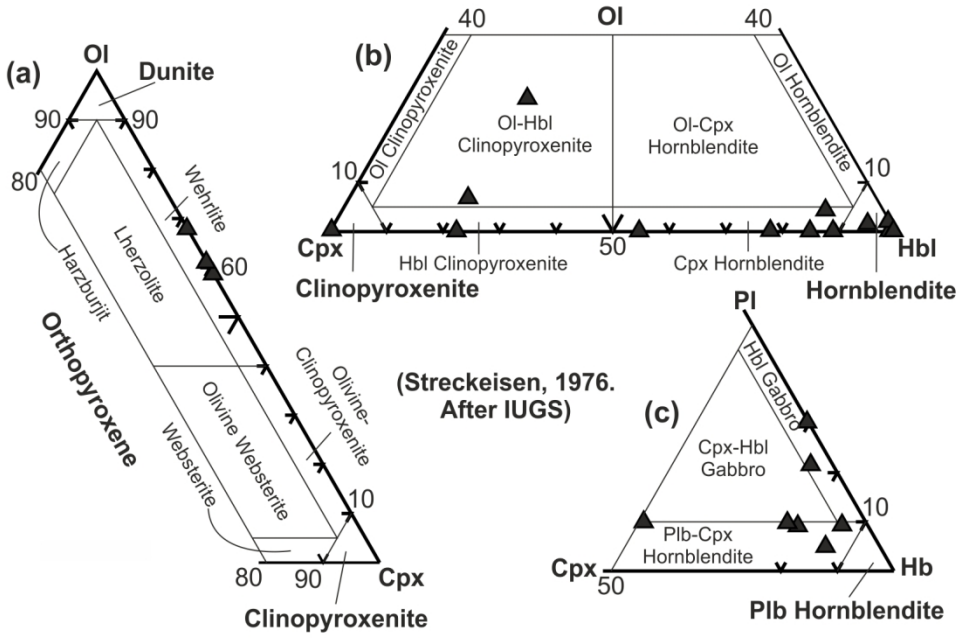

Figure 5

144x93mm (300 x 300 DPI)

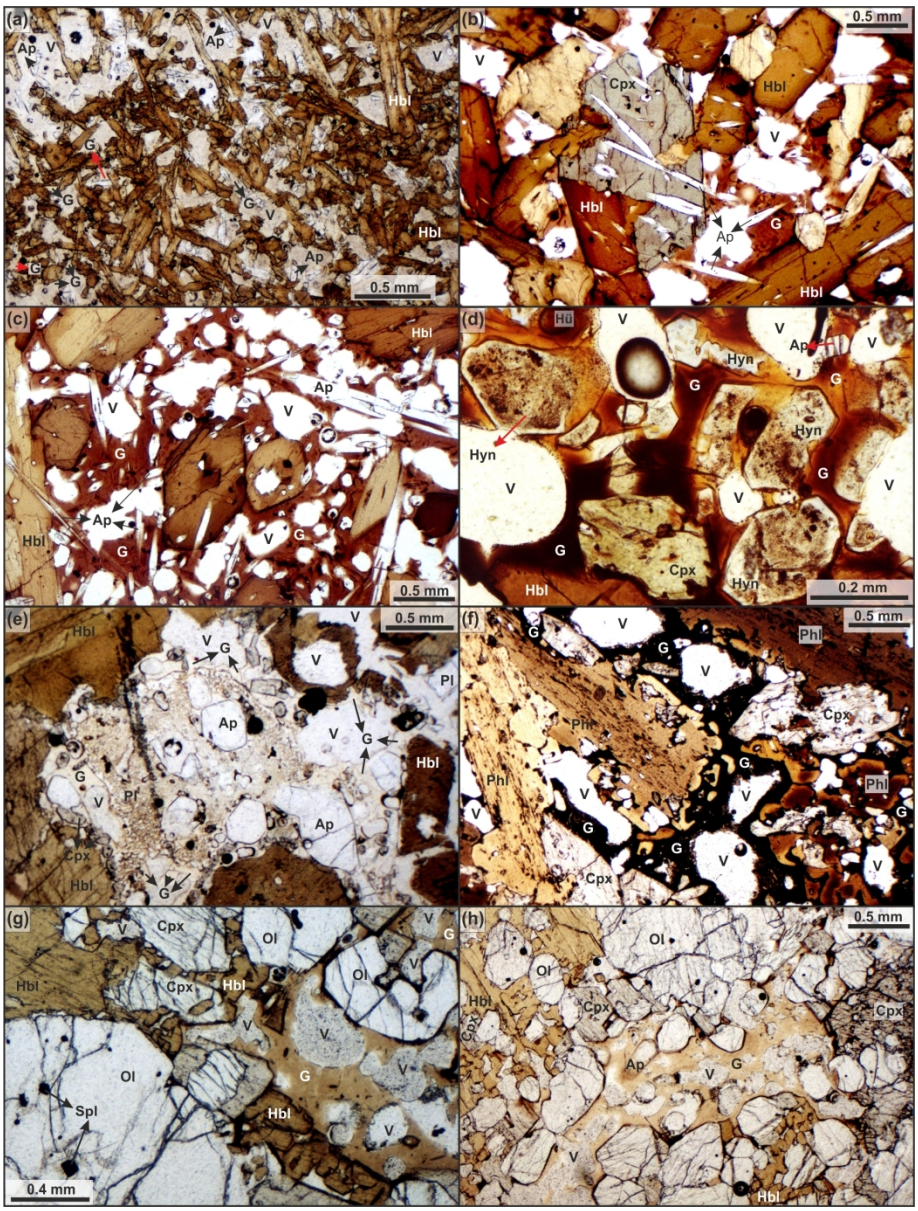

Figure 6

182x240mm (300 x 300 DPI)

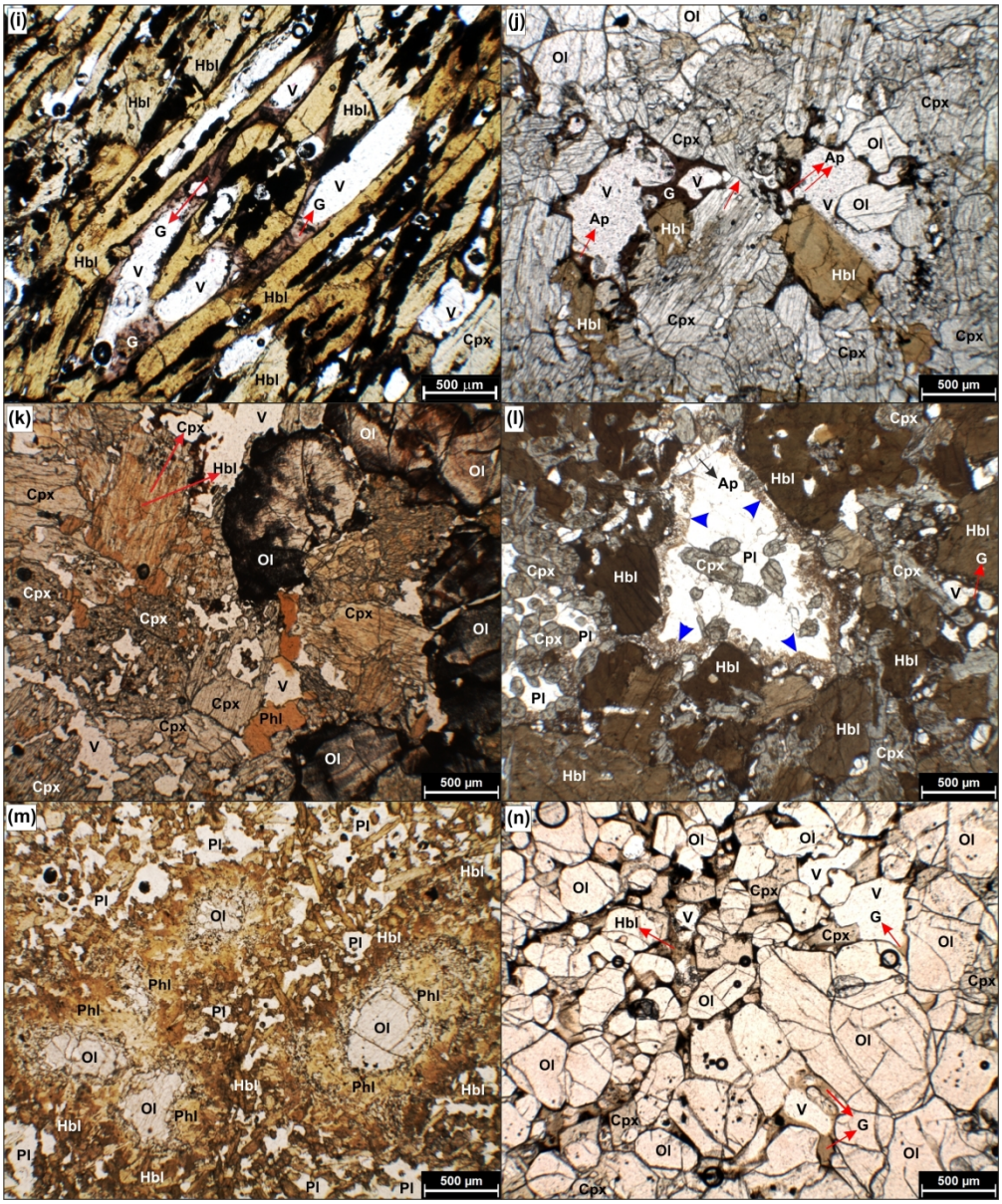

Figure 6 continued

191x229mm (300 x 300 DPI)

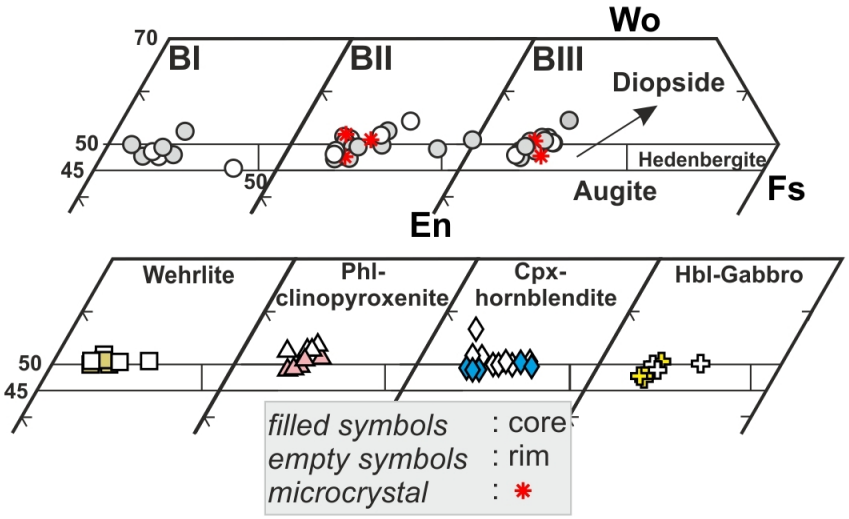

Figure 7

105x57mm (300 x 300 DPI)

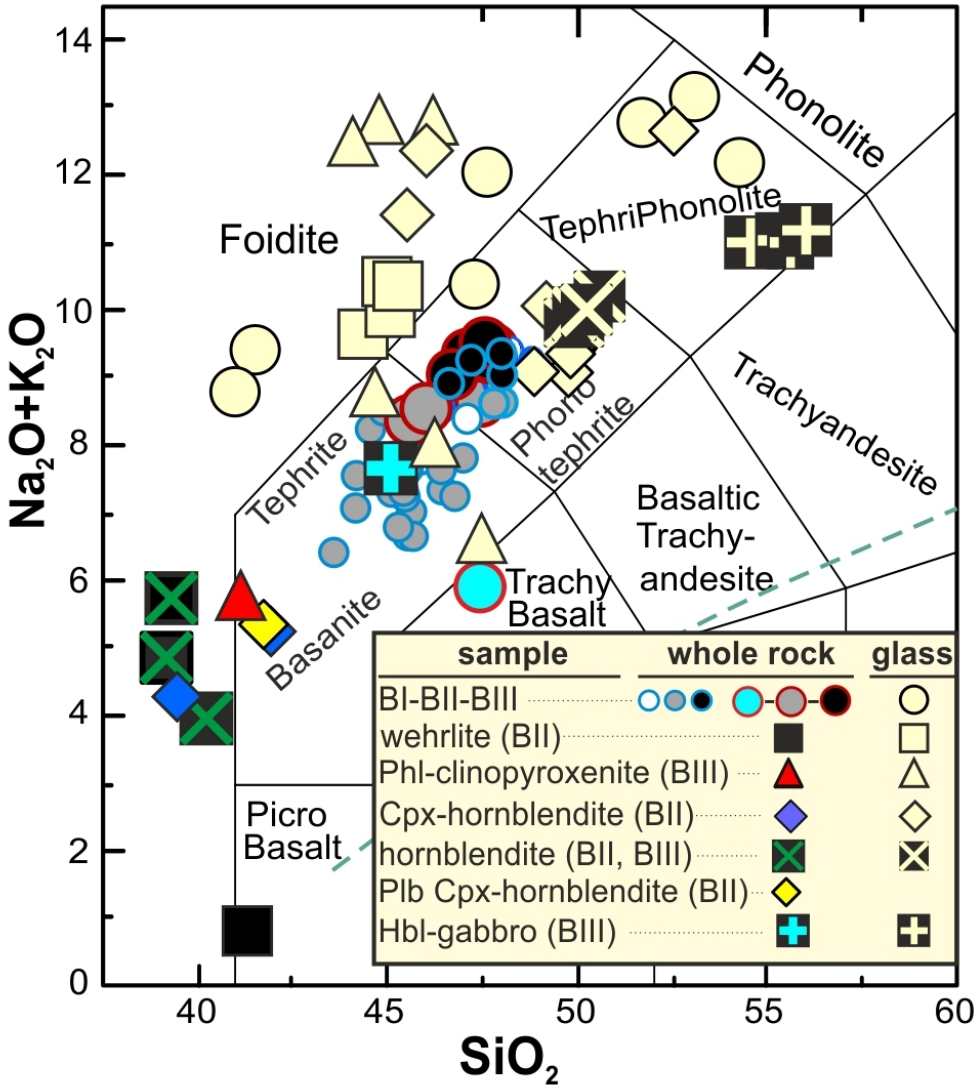

Figure 8

82x91mm (300 x 300 DPI)

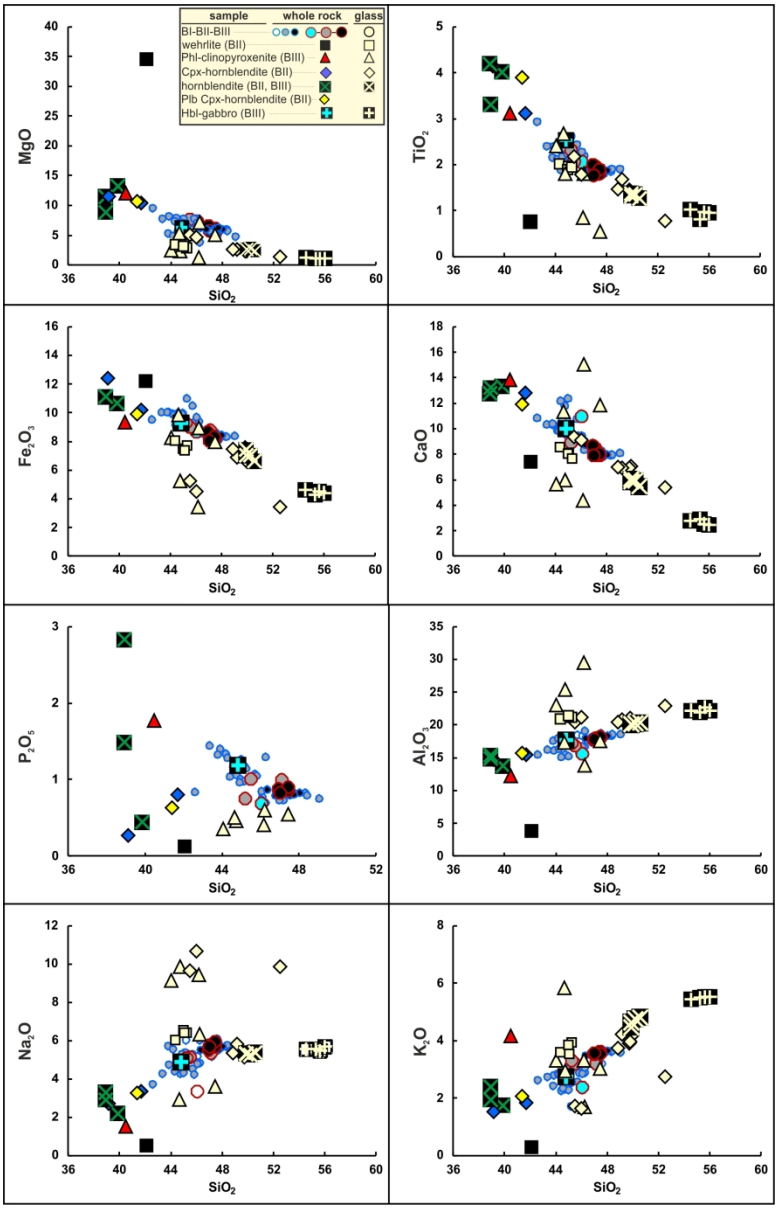

Figure 9

182x282mm (300 x 300 DPI)

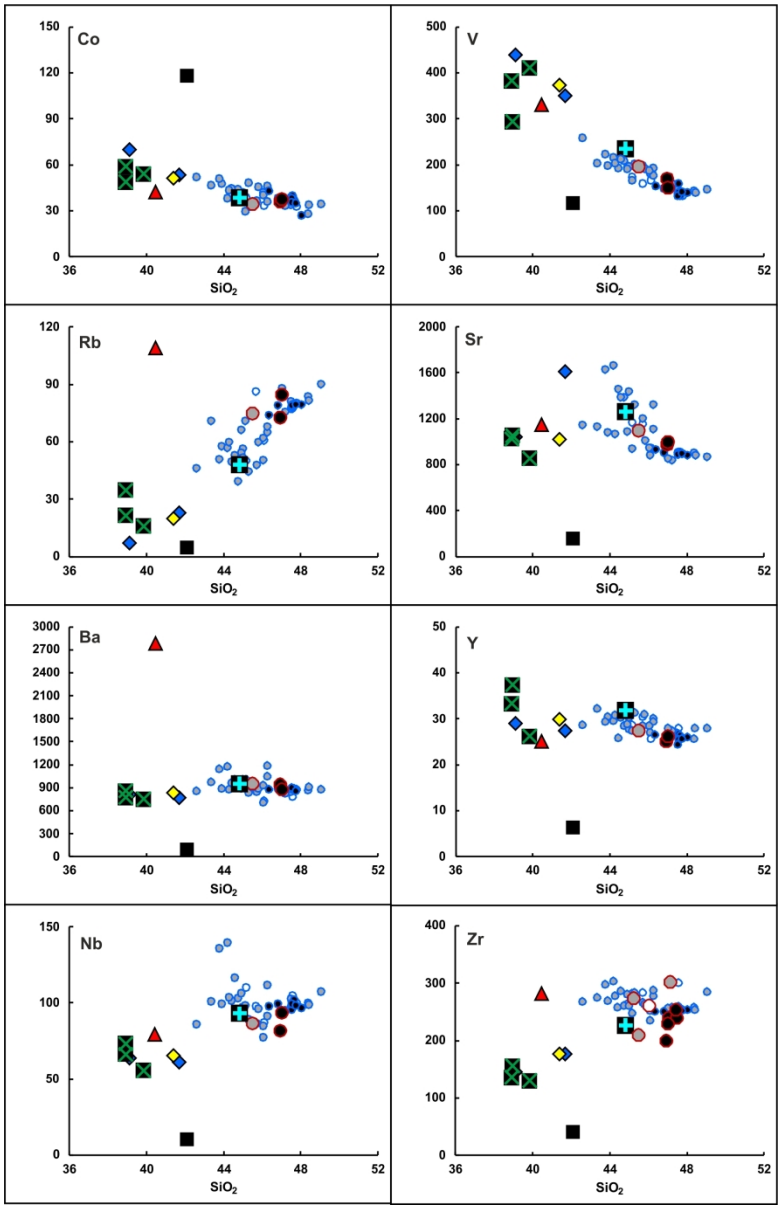

Figure 9 continued

182x281mm (300 x 300 DPI)

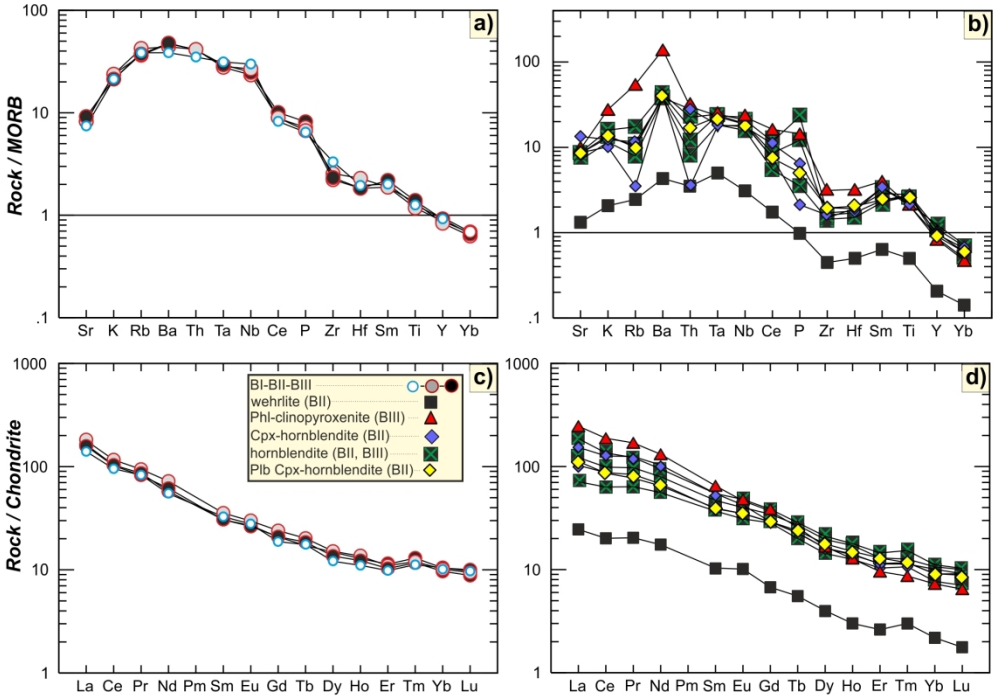

Figure 10

187x130mm (300 x 300 DPI)

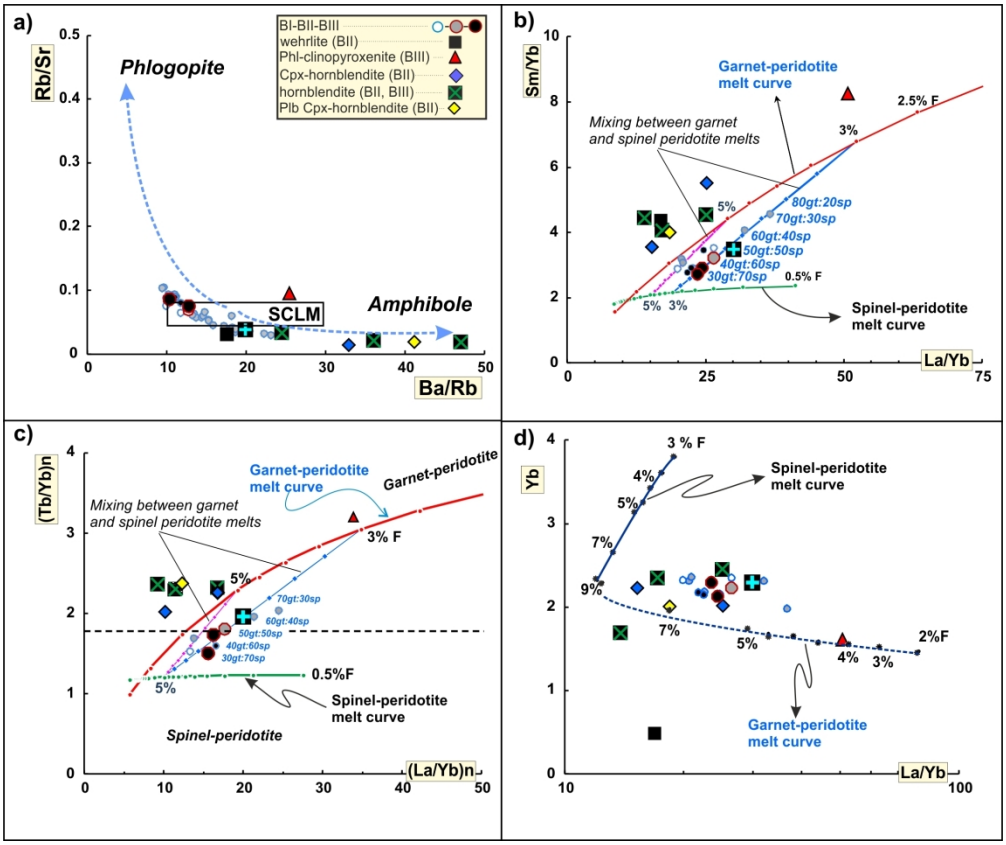

Figure 11

192x161mm (300 x 300 DPI)

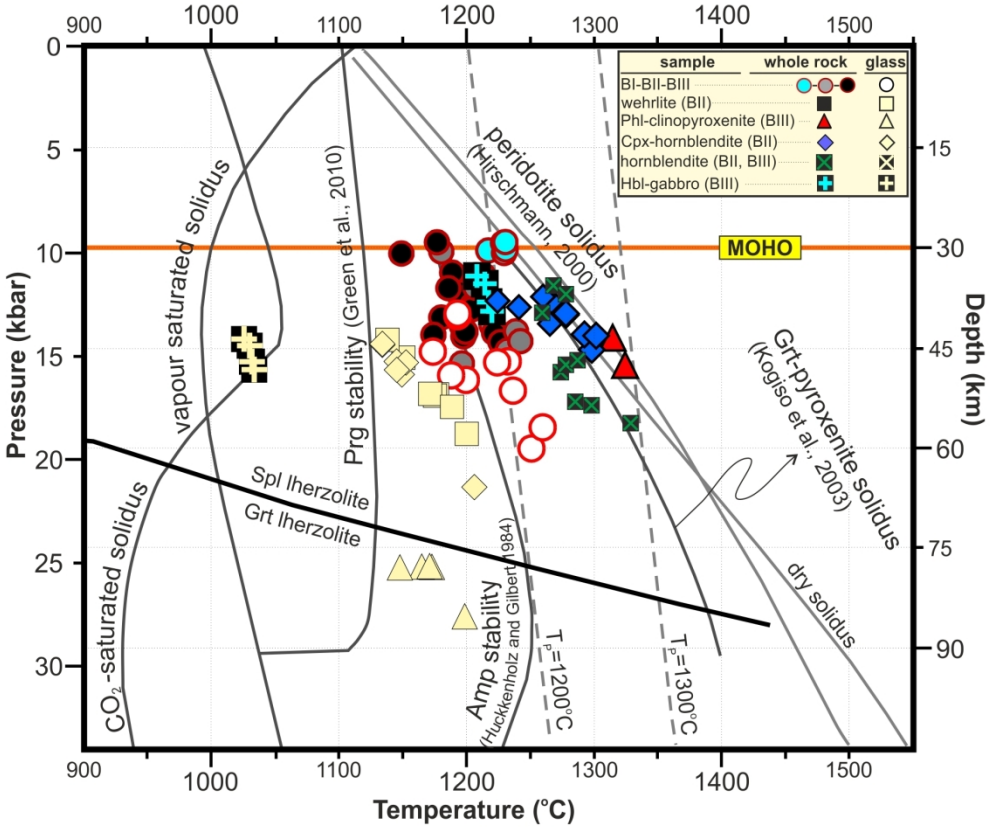

Figure 12

166x143mm (300 x 300 DPI)

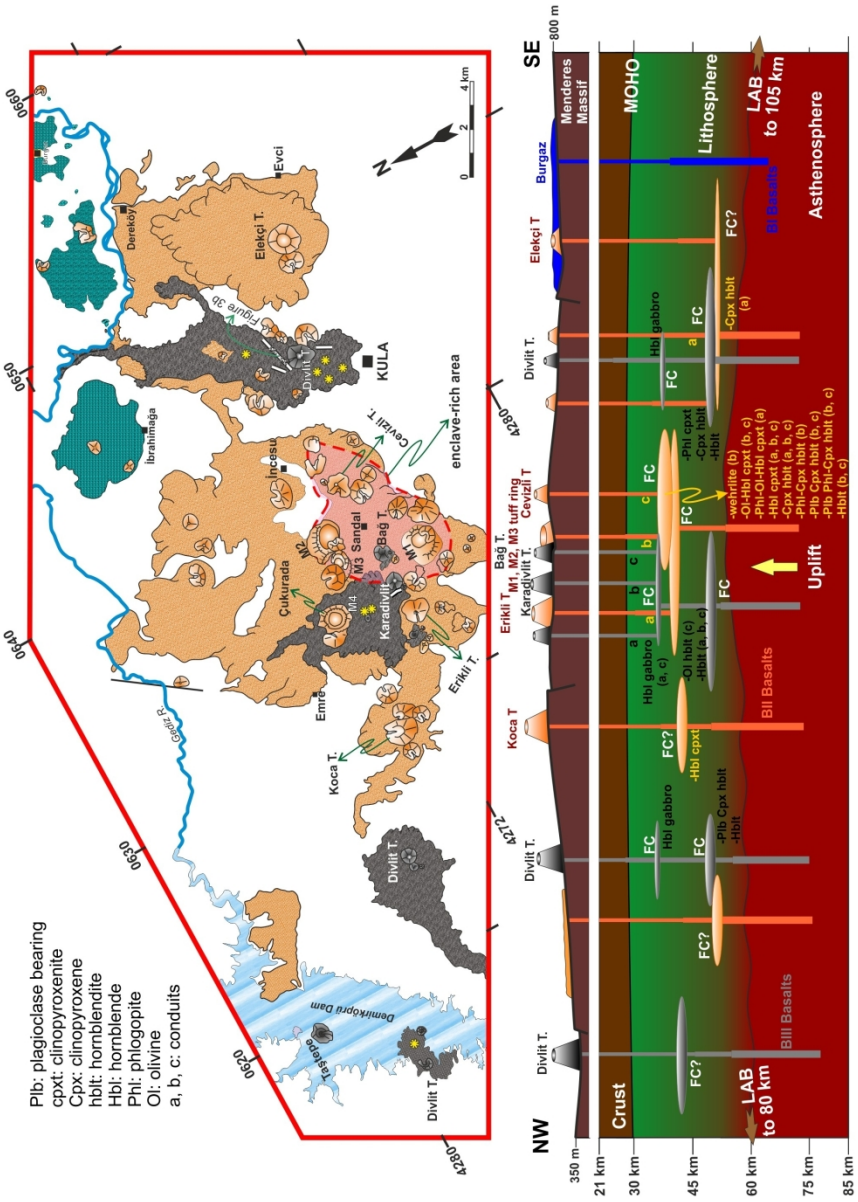

Figure 13

173x242mm (300 x 300 DPI)

UTM coordinates (WGS84, E / N)	637447 / 4272874				645204 / 4270729	635889 / 4269521	637447 / 4272874	639387 / 4271146	634570 / 4268542	637447 / 4272874	634570 / 4268542	637447 / 4272874
Sample No: K97-	**10a2(BII)**	**10a15(BII)**	**10a9(BII)**	**10a17(BII)**	**70a2(BIII)**	**49a3(BII)**	**10a16(BII)**	**30a(BII)**	**48a2(BII)**	**10a1(BII)**	**48a1(BII)**	**10a10(BII)**
# of points	*3000*	*3000*	*2890*	*2759*	*3000*	*2391*	*1000*	*3000*	*3151*	*1000*	*2061*	*2000*
Sample	**Wehrlite**	**Wehrlite**	**Wehrlite**	**Hbl-Cpxt**	**Phl-Cpxt**	**Ol-Hbl-Cpxt**	**Cpx-Hblt**	**Cpx-Hblt**	**Cpx-Hblt**	**Cpx-Hblt**	**Cpx-Hblt**	**Plb-Cpx-Hblt**
Olivine	56,9	54,8	50,3	-	-	6,7		-	-	-	3,25	-
Clinopyroxene	26,83	38,5	32	74	33	70,4	13,2	12,03	40,24	9,2	7,52	7,9
Hornblende	5,64	3,7	16,9	21,5	-	20,7	75,2	42,83	48,87	75,5	63,9	55,1
Phlogopite	-	-	0,3	0,2	38,5	-	-	-	-	2,1	-	18,1
Plagioclase	-	-	-	-	-	-	-	1,14	0,2	-	-	7
Nepheline	-	-	-	-	-	-	-	-	-	-	-	-
Haüyne	-	-	-	-	-	-	-	1,33	-	-	-	-
Apatite	-	-	-	-	1	0,1	3	1,67	0,06	-	-	6,5
Sphene	-	-	-	-	-	-	-	-	0,48	1,1	-	1,5
Calcite	-	0,5	-	-	-	-	-	-	-	-	-	-
Oxides	1,27	0,8	0,1	-	0,2	-	-	-	-	-	-	-
Total	***90,64***	***98,3***	***99,6***	***95,7***	***75,4***	***97,9***	***91,4***	***59***	***89,85***	***87,9***	***74,67***	***96,1***
Glass	5,8	0,6	0,3	3,2	13,9	1,3	5	19,03	6,09	4,1	11,45	1,8
Vesicle	3,56	1,1	0,1	1,1	10,7	0,8	3,6	21,97	4,06	8	13,88	2,1
Total	***9,36***	***1,7***	***0,4***	***4,3***	***24,6***	***2,1***	***8,6***	***41***	***10,15***	***12,1***	***25,33***	***3,9***

UTM coordinates (WGS84, E / N)	631879 / 4270995	644710 / 4269654	635889 / 4269521	634570 / 4268542	639684 / 4269941	624717 / 4275318	624717 / 4275318	637447 / 4272874		636125 / 4270660	632680 / 4271325
Sample No: K97-	**37a4(BII)**	**17a2(BIII)**	**49a1(BII)**	**14a(BIII)**	**33a(BII)**	**44a(BIII)**	**46a(BIII)**	**10a18(BII)**	**10a8(BII)**	**42a2(BIII)**	**39a1(BIII)**
# of points	*2006*	*3000*	*1077*	*2635*	*1000*	*2211*	*3300*	*2587*	*2000*	*2000*	*1000*
Sample	**Phl-Ol-Hbl Cpxt**	**Hblt**	**Hblt**	**Hblt**	**Hblt**	**Plb Cpx Hblt**	**Plb Cpx Hblt**	**Plb Phl-Cpx Hblt**	**Plb Phl-Cpx Hblt**	**Hbl Gabbro**	**Hbl Gabbro**
Olivine	22,9	-	0,8	-	1,2	0,5	-	-	-	0,8	-
Clinopyroxene	43,5	-	2	0,5	-	31,4	9	8,1	3,5	2,8	-
Hornblende	18,2	73,5	47,4	58,4	58,1	40,7	61,24	72,1	67,2	53,4	32,3
Phlogopite	13,2	-	-	-	1,9	1,2	-	6,4	6,9	0,8	-
Plagioclase	-	-	-	-	-	7,9	7,37	4,1	7,2	15,4	14
Apatite	0,4	3	1,4	7,1	4	0,7	1,21	0,5	4,9	2,6	3,7
Sphene	-	-	-	-	-	-	-	1,3	1,5	-	-
Total	***98,2***	***76,5***	***51,6***	***66***	***65,2***	***82,4***	***78,82***	***92,5***	***91,2***	***75,8***	***50***
Glass	1,1	11,5	17,9	17,7	14	9,4	11,57	4,3	4,1	11,3	29
Vesicle	0,7	12	30,5	16,3	20,8	8,2	9,61	3,2	4,7	12,9	21
Total	***1,8***	***23,5***	***48,4***	***34***	***34,8***	***17,6***	***21,18***	***7,5***	***8,8***	***24,2***	***50***

Ol: olivine, Cpx: clinopyroxene, Hbl: hornblende, Phl: phlogopite, Plb: plagioclase bearing, Cpxt: clinopyroxenite , Hblt: hornblendite

	Host rock																Enclave								
Olivine	BI			BII						BIII							Wehrlite (BII)				Hornblende Gabbro (BIII)				
Sample	K97-58			10			31		48			42			70		10a2				42a2				
	c	r	mc	c	r	mc	c	r	mc	c	r	c	r	mc	c	r	c	r	c	r	c	r	c	c	r
wt.%	#8	#9	58#	#6	#7	#22	#26	#27	#24	#26	#27	#33	#34	#42	#49	#50	#48	#49	#52	#53	#45	#46	#57	#61	#62
SiO_2	39,20	36,92	37,65	39,45	39,29	39,08	39,46	38,80	38,16	39,40	38,92	39,28	39,43	38,96	39,65	39,86	39,44	39,12	39,19	39,28	40,24	38,63	38,08	39,32	38,97
Al_2O_3	0,04	0,00	0,08	0,04	0,03	0,03	0,06	0,02	0,04	0,09	0,01	0,05	0,03	0,06	0,05	0,03	0,03	0,01	0,03	0,02	0,05	0,00	0,04	0,03	0,04
FeOt	14,92	25,74	26,75	12,34	12,77	13,62	12,87	14,20	18,47	15,72	17,49	14,16	14,34	14,28	13,63	13,07	14,79	14,98	14,70	14,30	13,90	18,29	19,81	14,50	15,38
MgO	46,21	37,38	35,19	47,35	46,87	46,01	47,39	45,87	42,03	44,90	43,42	46,27	45,86	45,81	47,62	47,22	45,80	46,07	45,81	45,79	46,10	42,29	40,65	46,11	45,09
CaO	0,29	0,40	0,39	0,21	0,25	0,25	0,22	0,25	0,28	0,25	0,29	0,22	0,22	0,27	0,24	0,18	0,08	0,09	0,09	0,15	0,25	0,21	0,21	0,23	0,11
Na_2O	0,00	0,04	0,02	0,03	0,03	0,02	0,01	0,00	0,00	0,04	0,00	0,00	0,00	0,02	0,03	0,00	0,01	0,02	0,04	0,04	0,02	0,00	0,01	0,01	0,01
K_2O	0,01	0,00	0,06	0,01	0,03	0,00	0,00	0,01	0,01	0,02	0,00	0,00	0,03	0,00	0,01	0,00	0,00	0,02	0,00	0,03	0,00	0,01	0,00	0,02	0,00
TiO_2	0,01	0,02	0,05	0,02	0,08	0,00	0,00	0,00	0,04	0,09	0,05	0,05	0,00	0,00	0,00	0,01	0,03	0,04	0,03	0,00	0,04	0,01	0,00	0,01	0,09
MnO	0,20	0,48	0,58	0,19	0,24	0,17	0,25	0,29	0,36	0,24	0,26	0,22	0,20	0,29	0,21	0,13	0,24	0,25	0,25	0,19	0,21	0,50	0,55	0,26	0,29
Cr_2O_3	0,05	0,00	0,00	0,03	0,04	0,03	0,00	0,02	0,02	0,03	0,00	0,02	0,00	0,05	0,00	0,01	0,02	0,00	0,01	0,00	0,00	0,00	0,00	0,03	0,11
NiO	0,05	0,03	0,00	0,19	0,18	0,14	0,13	0,14	0,06	0,08	0,08	0,09	0,12	0,11	0,05	0,14	0,11	0,09	0,14	0,13	0,11	0,09	0,09	0,15	0,10
Total	100,98	100,99	100,77	99,86	99,81	99,34	100,38	99,58	99,48	100,86	100,51	100,35	100,23	99,84	101,48	100,64	100,55	100,69	100,27	99,93	100,92	100,02	99,43	100,66	100,19
Calculation based on O=4 APFU																									
Si	0,977	0,972	0,995	0,983	0,982	0,985	0,981	0,979	0,983	0,986	0,986	0,982	0,987	0,980	0,978	0,987	0,986	0,979	0,983	0,987	0,997	0,988	0,988	0,982	0,982
Al	0,001	-	0,002	0,001	0,001	0,001	0,002	-	0,001	0,003	-	0,001	0,001	0,002	0,001	0,001	0,001	-	0,001	0,001	0,001	-	0,001	0,001	0,001
Fe	0,311	0,566	0,591	0,257	0,267	0,287	0,267	0,300	0,398	0,329	0,371	0,296	0,300	0,301	0,281	0,271	0,309	0,313	0,308	0,300	0,288	0,391	0,430	0,303	0,324
Mg	1,717	1,466	1,387	1,759	1,746	1,728	1,755	1,725	1,614	1,675	1,640	1,724	1,711	1,718	1,749	1,743	1,706	1,717	1,712	1,714	1,702	1,613	1,572	1,716	1,693
Ca	0,008	0,011	0,011	0,006	0,007	0,007	0,006	0,007	0,008	0,007	0,008	0,006	0,006	0,007	0,006	0,005	0,002	0,002	0,002	0,004	0,007	0,006	0,006	0,006	0,003
Na	-	0,002	0,001	0,001	0,002	0,001	0,001	-	-	0,002	-	-	-	0,001	0,001	-	-	0,001	0,002	0,002	0,001	-	0,001	0,001	-
K	-	-	0,002	-	0,001	-	-	-	-	0,001	-	-	0,001	-	-	-	-	0,001	-	0,001	-	-	-	0,001	-
Ti	-	-	0,001	-	0,002	-	-	-	0,001	0,002	0,001	0,001	-	-	-	-	0,001	0,001	0,001	-	0,001	-	-	-	0,002
Mn	0,004	0,011	0,013	0,004	0,005	0,004	0,005	0,006	0,008	0,005	0,006	0,005	0,004	0,006	0,004	0,003	0,005	0,005	0,005	0,004	0,004	0,011	0,012	0,005	0,006
Cr	0,001	-	-	0,001	0,001	0,001	-	-	-	0,001	-	-	-	0,001	-	-	-	-	-	-	-	-	-	0,001	0,002
Ni	0,001	0,001	-	0,004	0,004	0,003	0,003	0,003	0,001	0,002	0,002	0,002	0,002	0,002	0,001	0,003	0,002	0,002	0,003	0,003	0,002	0,002	0,002	0,003	0,002
Total	3,021	3,029	3,004	3,016	3,017	3,015	3,019	3,021	3,015	3,012	3,013	3,016	3,013	3,019	3,023	3,012	3,013	3,022	3,017	3,015	3,002	3,012	3,012	3,018	3,015
Mg#	85	72	70	87	87	86	87	85	80	84	82	85	85	85	86	87	85,00	85,00	85,00	85,00	86,00	80,00	79,00	85,00	84,00
Fo	84,7	72,1	70,1	87,2	86,7	85,8	86,8	85,2	80,2	83,6	81,6	85,3	85,1	85,1	86,2	86,6	84,7	84,6	84,7	85,1	85,5	80,5	78,5	85,0	83,9

c: core, r: rim, mc: microcrystal

	Host rock													Enclave										
Cpx	BI		BII					BIII						Wehrlite (BII)			Cpx-hornblendite (BII)					Hbl-gabbro (BIII)		Phl-clinopyroxenite	
Sample	K97-58		10		31			42		70				10a2			30a		48a			42a2		70a2	
	c	r	c	r	c	r	mc	c	r	c	r	mc	c	c in g	c	c in g	c in g	c	r	c in g	c	r	c	r
wt.%	#13	#14	#80	#81	#90	#91	#99	#45	#46	#56	#57	#67	#57	#67	#95	#5	#14	#132	#133	#152	#65	#66	#6	#7
SiO_2	52,18	49,32	44,57	47,74	45,83	48,74	47,86	48,82	49,37	40,85	46,37	45,66	47,39	43,69	46,41	45,62	45,95	46,41	45,80	49,42	49,44	48,97	51,90	44,90
Al_2O_3	0,66	2,82	7,25	5,37	9,26	6,49	6,44	5,62	4,91	12,92	7,71	8,88	6,28	9,83	9,39	8,97	9,52	8,98	8,71	6,07	5,78	6,17	4,10	9,62
FeOt	2,49	13,51	15,94	6,19	8,38	4,89	4,82	5,25	5,03	7,51	7,50	5,65	3,85	8,77	5,49	6,27	7,46	5,06	5,55	6,18	5,09	9,11	5,50	6,73
MgO	16,96	10,58	5,98	13,97	11,13	14,43	13,52	14,71	15,06	10,09	11,95	12,90	14,69	10,49	12,89	12,54	11,83	12,98	12,64	12,64	14,83	10,38	13,59	11,32
CaO	25,52	21,07	20,99	22,95	21,72	22,45	24,12	19,30	22,99	22,66	23,73	22,58	22,77	23,53	22,08	22,47	22,69	22,50	22,32	23,01	23,65	22,12	21,77	22,94	23,55
Na_2O	0,17	0,70	1,78	0,53	1,07	0,72	0,77	2,94	0,49	0,54	0,66	0,81	0,76	0,56	0,87	0,72	0,80	0,89	0,88	0,73	1,07	0,59	1,53	1,42	0,87
K_2O	0,01	0,02	0,00	0,01	0,02	0,00	0,00	0,00	0,01	0,01	0,00	0,03	0,03	0,02	0,04	0,02	0,01	0,01	0,03	0,04	0,00	0,00	0,01	0,02	0,01
TiO_2	0,12	1,13	1,92	1,98	2,33	1,77	1,74	0,46	1,79	1,42	3,04	1,89	2,43	1,72	3,00	2,80	2,19	2,04	2,34	2,63	1,12	1,62	1,57	0,69	3,25
MnO	0,38	0,41	0,59	0,11	0,12	0,08	0,10	0,35	0,08	0,13	0,08	0,15	0,04	0,05	0,44	0,09	0,12	0,13	0,12	0,12	0,14	0,12	0,24	0,14	0,17
Cr_2O_3	0,00	0,00	0,00	0,00	0,02	0,32	0,11	0,05	0,04	0,34	0,02	0,07	0,16	0,47	0,00	0,35	0,00	0,03	0,62	0,49	0,08	0,22	0,04	0,07	0,04
Total	98,50	99,57	99,02	98,85	99,87	99,88	99,49	98,47	99,80	99,48	98,91	99,05	99,30	98,56	99,20	100,63	99,21	100,36	99,75	99,71	100,37	99,81	99,79	100,37	100,44
Calculation based on O=6 APFU																									
Si	1,93	1,88	1,73	1,78	1,70	1,79	1,77	1,91	1,80	1,82	1,54	1,74	1,69	1,76	1,65	1,70	1,69	1,69	1,71	1,70	1,81	1,82	1,83	1,89	1,66
Mg	0,94	0,60	0,35	0,78	0,62	0,79	0,74	0,51	0,81	0,83	0,57	0,67	0,71	0,81	0,59	0,70	0,69	0,65	0,71	0,70	0,69	0,81	0,58	0,74	0,62
Ca	1,01	0,86	0,87	0,92	0,87	0,88	0,95	0,79	0,91	0,89	0,96	0,91	0,90	0,94	0,89	0,88	0,90	0,89	0,88	0,91	0,93	0,87	0,87	0,90	0,93
Na	0,01	0,05	0,13	0,04	0,08	0,05	0,06	0,22	0,04	0,04	0,05	0,06	0,06	0,04	0,06	0,05	0,06	0,06	0,06	0,05	0,08	0,04	0,11	0,10	0,06
K	0,00	0,00	0,00	0,00	0,00	0,00	0,00	0,00	0,00	0,00	0,00	0,00	0,00	0,00	0,00	0,00	0,00	0,00	0,00	0,00	0,00	0,00	0,00	0,00	0,00
Ti	0,00	0,03	0,06	0,06	0,07	0,05	0,05	0,01	0,05	0,04	0,09	0,05	0,07	0,05	0,09	0,08	0,06	0,06	0,07	0,07	0,03	0,05	0,04	0,02	0,09
Mn	0,01	0,01	0,02	0,00	0,00	0,00	0,00	0,01	0,00	0,00	0,00	0,01	0,00	0,00	0,01	0,00	0,00	0,00	0,00	0,00	0,00	0,00	0,01	0,00	0,01
Cr	0,00	0,00	0,00	0,00	0,00	0,01	0,00	0,00	0,00	0,01	0,00	0,00	0,01	0,01	0,00	0,01	0,00	0,00	0,02	0,01	0,00	0,01	0,00	0,00	0,00
Fe3+	0,08	0,10	0,23	0,13	0,13	0,09	0,14	0,23	0,10	0,10	0,23	0,14	0,15	0,12	0,17	0,08	0,16	0,15	0,11	0,12	0,12	0,07	0,09	0,10	0,15
Fe2+	0,00	0,33	0,29	0,06	0,13	0,06	0,00	0,19	0,06	0,05	0,01	0,09	0,03	0,00	0,11	0,08	0,04	0,08	0,05	0,05	0,07	0,09	0,19	0,07	0,06
Al_{IV}	0,03	0,12	0,27	0,22	0,30	0,21	0,24	0,09	0,21	0,18	0,47	0,27	0,31	0,24	0,36	0,30	0,31	0,31	0,29	0,31	0,19	0,19	0,17	0,11	0,34
Al_{VI}	0,00	0,01	0,06	0,02	0,11	0,07	0,05	0,05	0,04	0,03	0,11	0,08	0,08	0,04	0,08	0,10	0,09	0,11	0,10	0,07	0,08	0,07	0,10	0,07	0,08
Total	4,02	4,00	4,00	4,00	4,00	4,00	4,00	4,00	4,00	4,00	4,00	4,00	4,00	4,01	4,00	4,00	4,00	4,00	4,00	4,00	4,00	4,00	4,00	4,00	4,00
Fe2O3	2,77	3,41	7,94	4,66	4,70	3,22	5,21	8,05	3,68	3,62	8,13	5,03	5,21	4,28	5,93	3,06	5,53	5,32	3,83	4,42	4,41	2,40	3,27	3,56	5,21
FeO	0,00	10,44	8,80	2,00	4,15	1,98	0,13	5,90	1,94	1,76	0,20	2,98	0,97	0,00	3,43	2,74	1,29	2,67	1,61	1,57	2,21	2,94	6,17	2,29	2,04
Wo	49,97	45,47	50,26	48,60	49,65	48,46	51,66	45,99	48,35	47,67	54,39	50,12	50,46	50,09	50,73	50,28	50,40	50,24	50,35	51,23	51,34	47,35	50,24	49,72	52,87
En	46,21	31,77	19,93	41,16	35,40	43,31	40,29	29,56	43,03	44,08	32,17	36,88	39,77	43,51	33,54	40,12	38,73	36,76	40,74	39,14	38,19	44,15	33,34	40,98	35,34
Fs	3,81	22,76	29,81	10,24	14,95	8,23	8,05	24,45	8,62	8,25	13,44	13,00	9,77	6,40	15,73	9,60	10,87	13,00	8,91	9,63	10,48	8,51	16,41	9,30	11,79
Mg*	92	58	40	80	70	84	83	55	83	84	71	74	80	87	68	81	78	74	82	80	78	84	67	82	75

c: core, r: rim, mc: microcrystal, g: glass, Hbl: hornblend, Cpx: clinopyroxene, Phl: phlogopite

(BIII)
r
#11
42,14
12,32
6,80
10,80
24,29
0,49
0,01
3,12
0,10
0,04
100,08
1,56
0,60
0,97
0,04
0,00
0,09
0,00
0,00
0,20
0,02
0,44
0,10
4,00
6,98
0,52
54,45
33,66
11,89
74

	Host rock												Enclave														
Hbl	BII			BIII									Wehrlite (BII)		Hornblendite (BIII)			Clinopyroxene hornblendite (BII)							Hbl-Gabbro (BIII)		
Sample	K97-10			31			42		70				10a2		17a2			30a					48a			42a2		
	c	r	m	c	m	m	c	r	c	m	c	r	c	r	c	r	inc	c	r	inc	c in g	c	c	r	c	c	c in g	c
wt.%	#92	#93	#96	#1	#12	#21	#34b	#35b	#39b	#59	#47b	#48b	#64	#65	#34	#35	#40	#18	#19	#20	#103	#107	#129	#130	#147	#42	#54	#58
SiO_2	38,71	37,90	37,21	38,28	40,48	40,96	38,98	38,04	39,24	39,33	37,94	38,45	38,74	39,18	39,74	39,03	38,60	37,65	38,64	37,93	38,98	40,57	38,83	39,44	39,40	39,75	38,83	38,11
Al_2O_3	13,86	14,30	14,49	14,80	11,92	10,85	14,73	14,59	14,58	14,21	14,07	14,49	14,82	14,09	14,55	14,03	14,05	14,34	14,52	15,09	14,94	14,54	14,59	15,07	14,71	14,18	14,54	15,35
FeOt	11,06	11,11	16,21	8,04	7,40	9,52	8,17	8,74	8,39	9,92	16,97	10,10	13,91	8,25	8,19	11,14	14,32	11,70	9,12	14,59	8,74	8,14	7,86	10,06	7,82	7,89	9,51	13,75
MgO	13,20	12,41	8,88	14,03	10,36	9,21	14,23	13,85	13,93	13,44	8,43	12,77	10,78	14,65	13,92	12,39	10,73	12,13	13,33	10,25	13,97	14,41	14,25	13,49	14,62	13,94	12,90	10,39
CaO	12,22	11,99	11,45	12,27	22,18	21,55	12,39	11,86	12,28	11,98	11,74	11,90	11,16	12,19	11,84	12,13	11,61	11,77	11,89	11,78	11,84	12,23	12,07	12,17	12,21	11,50	11,83	11,70
Na_2O	2,49	2,27	2,61	2,09	0,86	1,02	2,24	2,20	2,43	2,46	2,34	2,24	2,49	2,34	2,44	2,50	2,46	2,86	2,84	2,71	3,02	2,45	2,59	2,46	2,46	2,92	2,69	2,70
K_2O	1,78	1,49	1,77	2,07	0,05	0,03	1,81	1,88	1,73	1,69	1,78	1,64	2,03	1,75	1,73	1,89	1,72	1,62	1,55	1,63	1,33	1,53	1,82	2,07	1,71	1,53	1,50	1,44
TiO_2	4,37	5,46	4,71	5,27	4,34	3,66	5,15	5,30	5,35	4,19	3,95	4,78	3,05	4,53	5,38	4,42	4,24	3,83	4,27	3,58	4,42	4,31	4,78	2,30	5,12	5,49	5,26	3,70
MnO	0,20	0,10	0,31	0,04	0,11	0,18	0,10	0,10	0,07	0,12	0,25	0,15	0,21	0,06	0,07	0,10	0,19	0,18	0,13	0,27	0,13	0,15	0,10	0,09	0,08	0,10	0,16	0,23
Cr_2O_3	0,03	0,00	0,00	0,04	0,02	0,08	0,00	0,00	0,00	0,02	0,00	0,00	0,03	0,08	0,02	0,00	0,03	0,02	0,03	0,00	0,00	0,00	0,09	0,10	0,03	0,13	0,01	0,04
Tot	97,91	97,02	97,65	96,92	97,70	97,05	97,78	96,56	98,00	97,36	97,46	96,53	97,22	97,10	97,87	97,64	97,96	96,09	96,32	97,82	97,37	98,33	96,97	97,24	98,15	97,41	97,24	97,40
	Calculation based on O=23 APFU																											
Si	5,77	5,69	5,70	5,69	6,01	6,17	5,73	5,68	5,76	5,84	5,83	5,77	5,87	5,80	5,82	5,83	5,82	5,74	5,79	5,74	5,76	5,90	5,75	5,87	5,75	5,84	5,77	5,76
Mg	2,93	2,78	2,03	3,11	2,29	2,07	3,12	3,09	3,05	2,98	1,93	2,86	2,43	3,23	3,04	2,76	2,41	2,76	2,98	2,31	3,07	3,12	3,15	2,99	3,18	3,05	2,86	2,34
Ca	1,95	1,93	1,88	1,95	3,53	3,48	1,95	1,90	1,93	1,91	1,93	1,91	1,81	1,93	1,86	1,94	1,88	1,92	1,91	1,91	1,87	1,90	1,92	1,94	1,91	1,81	1,88	1,89
Na	0,72	0,66	0,78	0,60	0,25	0,30	0,64	0,64	0,69	0,71	0,70	0,65	0,73	0,67	0,69	0,72	0,72	0,84	0,83	0,80	0,86	0,69	0,74	0,71	0,70	0,83	0,77	0,79
K	0,34	0,29	0,35	0,39	0,01	0,01	0,34	0,36	0,32	0,32	0,35	0,31	0,39	0,33	0,32	0,36	0,33	0,32	0,30	0,31	0,25	0,28	0,34	0,39	0,32	0,29	0,28	0,28
Ti	0,49	0,62	0,54	0,59	0,48	0,41	0,57	0,60	0,59	0,47	0,46	0,54	0,35	0,50	0,59	0,50	0,48	0,44	0,48	0,41	0,49	0,47	0,53	0,26	0,56	0,61	0,59	0,42
Mn	0,03	0,01	0,04	0,00	0,01	0,02	0,01	0,01	0,01	0,01	0,03	0,02	0,03	0,01	0,01	0,01	0,02	0,02	0,02	0,03	0,02	0,02	0,01	0,01	0,01	0,01	0,02	0,03
Cr	0,00	0,00	0,00	0,00	0,00	0,01	0,00	0,00	0,00	0,00	0,00	0,00	0,00	0,01	0,00	0,00	0,00	0,00	0,00	0,00	0,00	0,00	0,01	0,01	0,00	0,01	0,00	0,00
Fe 3+	0,13	0,09	0,02	0,00	0,00	0,00	0,00	0,14	0,00	0,08	0,00	0,05	0,31	0,11	0,00	0,00	0,16	0,11	0,00	0,13	0,07	0,00	0,00	0,17	0,00	0,00	0,00	0,09
Fe2+	1,25	1,31	2,05	1,00	0,92	1,20	1,00	0,95	1,03	1,15	2,18	1,22	1,45	0,91	1,00	1,39	1,65	1,39	1,14	1,71	1,01	0,99	0,97	1,09	0,96	0,97	1,18	1,65
Al_{IV}	2,25	2,32	2,30	2,30	1,38	1,21	2,26	2,33	2,22	2,17	2,16	2,24	2,17	2,21	2,17	2,15	2,20	2,27	2,20	2,27	2,25	2,10	2,24	2,15	2,25	2,14	2,21	2,25
Al_{VI}	0,18	0,21	0,31	0,29	0,91	0,91	0,29	0,23	0,31	0,32	0,39	0,32	0,46	0,24	0,35	0,33	0,29	0,30	0,37	0,41	0,35	0,39	0,32	0,49	0,29	0,33	0,34	0,48
Tot	16,04	15,89	16,01	15,93	15,80	15,79	15,92	15,92	15,91	15,95	15,96	15,89	16,00	15,96	15,85	15,99	15,96	16,11	16,01	16,05	16,00	15,87	15,98	16,08	15,92	15,89	15,91	15,98
Mg#	68	66	49	76	71	63	75	74	75	70	47	69	58	76	75	66	57	65	72	55	74	76	76	70	77	76	70	57
Naming	Prg	Krs	Krs	Krs	Prg	Prg	Krs	Krs	Krs	Prg	Prg	Krs	Prg	Krs	Krs	Prg	Prg	Prg	Krs	Prg	Prg	Prg	Krs	Prg	Krs	Krs	Krs	Prg

c: core, r: rim, mc: microcrystal, g: glass, inc: inclusion, Prg: pargasite, Krs: kaersutite, Hbl: hornblend

Phl	Phl-clinopyroxenite (BIII)				Hbl-Gabbro (BIII)	
Sample	K97-70a2				42a2	
	c	r	c	r	mc	mc
wt.%	#4	#5	#12	#13	#48	#60
SiO_2	36,44	35,63	36,27	36,38	38,45	37,40
Al_2O_3	17,17	16,95	15,81	17,21	14,69	15,78
FeOt	11,82	10,23	12,21	9,64	7,73	9,67
MgO	16,84	17,60	17,06	18,44	21,41	18,86
CaO	0,03	0,10	0,00	0,05	0,06	0,07
Na_2O	0,46	0,46	0,51	0,61	0,86	0,96
K_2O	9,67	9,67	9,56	9,34	9,06	9,02
TiO_2	3,95	4,33	2,58	3,33	2,96	3,27
MnO	0,19	0,14	0,17	0,14	0,11	0,12
Total	96,57	95,11	94,17	95,15	95,33	95,14
Calculation based on O=22 APFU						
Si	5,73	5,66	5,83	5,73	6,05	5,95
Al	3,18	3,17	2,99	3,19	2,73	2,96
Fe3+	0,49	0,59	0,85	0,64	0,77	0,65
Fe2+	1,07	0,77	0,79	0,63	0,23	0,62
Mg	3,95	4,16	4,09	4,33	5,02	4,47
Ca	0,01	0,02	0,00	0,01	0,01	0,01
Na	0,14	0,14	0,16	0,19	0,26	0,30
K	1,94	1,96	1,96	1,88	1,82	1,83
Ti	0,47	0,52	0,31	0,39	0,35	0,39
Mn	0,03	0,02	0,02	0,02	0,01	0,02
Fe	1,56	1,36	1,64	1,27	1,02	1,29
Total	17,00	17,00	17,00	17,00	17,26	17,22
Fe2O3	4,13	4,91	7,04	5,36	6,62	5,49
FeO	8,11	5,82	5,87	4,82	1,77	4,73
Mg/Fe	2,54	3,07	2,49	3,41	4,94	3,47
Fe#	0,28	0,25	0,29	0,23	0,17	0,22

c: core, r: rim, mc: microcrystal

	Host rock											Enclave						
Pl	BI			BII			BIII					Hornblende gabbro (BIII)				Cpx-hornblendite (BII)		
Sample	K97-58			31	48		42		70			K97-42a2				K97-48a		
	c	r	m	m	m	m	m	m	m	c	r	c	m	m	m	c	c	r
wt.%	#10b	#11b	#2b	#14	#23	#37b	#40b	#70	#82	#42b	#43b	#43	#55	#67	#70	#140	#141	#142
SiO_2	53,54	52,89	50,95	54,12	51,45	53,71	52,12	53,02	54,17	55,85	54,95	55,83	55,78	56,42	57,50	44,36	51,50	43,70
Al_2O_3	28,94	29,29	30,08	27,11	29,13	28,36	30,02	28,32	25,90	28,19	28,66	27,10	27,04	26,96	26,70	34,09	29,21	35,06
FeOt	0,38	0,34	0,69	0,49	0,46	0,68	0,63	0,55	1,25	0,21	0,32	0,29	0,23	0,27	0,25	0,18	0,56	0,23
MgO	0,03	0,05	0,07	0,03	0,01	0,04	0,05	0,14	0,62	0,01	0,03	0,03	0,01	0,02	0,00	0,03	0,03	0,00
CaO	11,47	11,73	12,93	9,31	11,86	10,53	11,88	11,04	9,87	9,59	10,58	9,47	9,35	8,73	8,54	17,96	12,05	18,70
Na_2O	4,67	4,50	3,88	5,94	4,68	5,28	4,38	4,95	6,13	5,62	5,31	5,89	5,94	6,19	6,16	1,17	4,55	0,69
K_2O	0,64	0,61	0,45	0,61	0,26	0,43	0,46	0,61	0,89	0,65	0,58	0,58	0,69	0,66	0,66	0,06	0,26	0,04
TiO_2	0,08	0,09	0,16	0,11	0,20	0,17	0,12	0,08	0,53	0,05	0,00	0,03	0,03	0,04	0,04	0,03	0,20	0,07
Total	99,74	99,49	99,20	97,71	98,04	99,18	99,66	98,71	99,36	100,16	100,43	99,21	99,06	99,27	99,84	97,88	98,35	98,49
Calculation based on O=32 APFU																		
Si	9,74	9,65	9,37	10,01	9,54	9,81	9,51	9,75	9,96	10,04	9,89	10,14	10,15	10,22	10,33	8,37	9,53	8,20
Al	6,20	6,30	6,53	5,91	6,37	6,11	6,46	6,14	5,61	5,97	6,08	5,80	5,80	5,76	5,66	7,58	6,37	7,76
Fe	0,06	0,05	0,11	0,08	0,07	0,10	0,10	0,08	0,19	0,03	0,05	0,05	0,04	0,04	0,04	0,03	0,09	0,04
Mg	0,01	0,01	0,02	0,01	0,00	0,01	0,01	0,04	0,17	0,00	0,01	0,01	0,00	0,01	0,00	0,01	0,01	0,00
Ca	2,23	2,29	2,55	1,84	2,36	2,06	2,32	2,18	1,94	1,85	2,04	1,84	1,82	1,70	1,64	3,63	2,39	3,76
Na	1,64	1,59	1,38	2,13	1,68	1,87	1,55	1,77	2,19	1,96	1,85	2,07	2,09	2,18	2,15	0,43	1,63	0,25
K	0,15	0,14	0,11	0,15	0,06	0,10	0,11	0,14	0,21	0,15	0,13	0,13	0,16	0,15	0,15	0,01	0,06	0,01
Ti	0,01	0,01	0,02	0,02	0,03	0,02	0,02	0,01	0,07	0,01	0,00	0,00	0,00	0,01	0,01	0,01	0,03	0,01
Total	20,04	20,05	20,08	20,14	20,12	20,08	20,07	20,12	20,35	20,01	20,05	20,05	20,07	20,05	19,98	20,06	20,10	20,03
An	56,8	58,3	64,4	46,1	58,8	52,6	59,7	54,6	46,2	48,1	52,0	46,9	46,1	43,5	43,0	89,7	59,9	93,9
Ab	39,4	38,1	32,9	50,2	39,6	44,9	37,6	41,8	48,9	48,0	44,5	49,7	49,9	52,6	53,0	10,0	38,5	5,9
Or	3,8	3,6	2,7	3,6	1,6	2,5	2,7	3,6	5,0	3,9	3,4	3,4	4,0	3,9	4,0	0,3	1,5	0,2

c: core, r: rim, m: microlite

Nepheline

	BII				BIII	Hbl-clinopyroxenite (BII)		
Sample	K97-31	48			70	31a		
	m	m	c	r	c	c	c	c
wt.%	#13	#15b	#17b	#18b	#83	#33	#38	#45
SiO_2	43,37	43,98	44,07	43,05	52,76	43,31	43,11	42,85
Al_2O_3	28,18	33,85	33,86	34,12	25,85	34,23	34,19	33,50
FeOt	3,29	0,58	0,20	0,23	2,56	0,15	0,14	0,14
MgO	1,17	0,00	0,04	0,02	0,28	0,02	0,01	0,00
CaO	4,79	1,48	1,80	1,25	0,54	2,58	2,73	2,04
Na_2O	14,23	15,43	15,82	16,21	13,24	15,75	15,94	16,03
K_2O	2,39	4,04	4,16	4,37	1,67	4,35	3,84	4,37
TiO_2	1,45	0,07	0,00	0,00	0,77	0,00	0,01	0,00
Total	98,85	99,43	99,95	99,24	97,67	100,40	99,97	98,93
	Calculation based on O=32 APFU							
Si	8,48	8,40	8,39	8,27	9,96	8,24	8,23	8,28
Al	6,49	7,62	7,60	7,73	5,75	7,68	7,69	7,63
Fe	0,54	0,09	0,03	0,04	0,40	0,03	0,02	0,02
Mg	0,34	0,00	0,01	0,01	0,08	0,00	0,00	0,00
Ca	1,00	0,30	0,37	0,26	0,11	0,53	0,56	0,42
Na	5,39	5,72	5,84	6,04	4,85	5,81	5,90	6,01
K	0,60	0,98	1,01	1,07	0,40	1,06	0,94	1,08
Ti	0,21	0,01	0,00	0,00	0,11	0,00	0,00	0,00
Total	23,06	23,13	23,24	23,42	21,68	23,35	23,34	23,44

	Leucite				Hauyne			
	BI	BII	BIII		Cpx-hornblendite (BII)			
Sample	56	48	42	70	30a			
	c	c	m	c	c	c	c	c
wt.%	16	#28	#30	#81	#2	#3	#12	#105
SiO_2	54,87	54,39	55,04	54,40	34,37	35,68	34,11	34,02
Al_2O_3	22,94	23,10	24,26	23,51	28,12	26,78	27,29	28,13
FeOt	0,42	0,27	0,23	0,29	0,23	0,57	0,21	0,80
MgO	0,01	0,00	0,00	0,01	0,23	0,25	0,16	0,22
CaO	0,00	0,00	0,06	0,04	7,57	6,78	7,59	7,71
Na_2O	0,09	0,29	0,50	0,10	10,35	7,26	8,07	8,36
K_2O	21,20	21,11	19,49	21,32	4,29	5,40	5,28	6,30
TiO_2	0,12	0,16	0,00	0,24	0,02	0,00	0,06	0,00
Total	99,76	99,32	99,57	99,92	85,17	82,71	82,75	85,55
	Calc. based on O=32 APFU				Calc. based on O=21 APFU			
Si	2,00	1,99	1,99	1,98	5,16	5,46	5,26	5,13
Al	0,99	1,00	1,03	1,01	4,97	4,83	4,95	5,00
Fe	0,01	0,01	0,01	0,01	0,03	0,07	0,03	0,10
Mg	0,00	0,00	0,00	0,00	0,05	0,06	0,04	0,05
Ca	0,00	0,00	0,00	0,00	1,22	1,11	1,25	1,25
Na	0,01	0,02	0,04	0,01	3,01	2,15	2,41	2,44
K	0,99	0,99	0,90	0,99	0,82	1,05	1,04	1,21
Ti	0,00	0,00	0,00	0,01	0,00	0,00	0,01	0,00
Total	4,00	4,01	3,96	4,01	15,27	14,73	14,98	15,19

c: core, r: rim, m: microlite

Oxides	Host rock BI			BIII			Enclave Wehrlite (BII)						Cpx-hornblendite	
Sample	**K97-58**			**70**			**10a2**						**48a**	
	Titanomagnetite			**Spinel**			**Chromian spinel**						**Magnesian ilmenit**	
	mc	mc	mc	inc	inc	inc	mp	inc	inc	inc	inc	inc	c	c
wt.%	#5	#6	#7	#66	#78	#79	#86	#50	#51	#54	#55	#56	#155	#156
SiO_2	0,10	0,10	0,07	0,05	0,12	0,11	0,02	0,05	0,02	0,00	0,00	0,03	0,24	0,42
Al_2O_3	4,10	4,09	3,68	55,08	59,64	59,65	61,19	38,13	37,98	32,42	32,39	36,52	0,41	0,24
FeOt	65,78	64,87	65,64	27,54	19,19	19,54	28,64	25,50	25,70	24,33	25,05	25,23	33,28	33,15
MgO	4,21	3,95	3,85	16,19	20,08	19,88	9,60	14,89	14,59	13,85	13,72	13,70	8,42	8,46
CaO	0,16	0,24	0,14	0,02	0,04	0,00	0,04	0,00	0,04	0,02	0,00	0,01	0,02	0,16
Na_2O	23,14	23,05	22,23	1,04	0,95	1,17	0,31	1,41	1,42	0,86	0,90	0,87	53,74	53,46
MnO	0,69	0,72	0,76	0,27	0,06	0,07	0,26	0,15	0,13	0,07	0,06	0,16	0,49	0,39
Cr_2O_3	0,09	0,04	0,02	0,05	0,01	0,04	0,00	18,97	19,03	27,21	26,89	22,33	0,02	0,05
Total	98,28	97,07	96,38	100,25	100,10	100,46	100,06	99,10	98,91	98,76	99,00	98,84	96,61	96,32
				Calculation based on O=32 APFU										**O=6 APFU**
Si	0,03	0,03	0,02	0,01	0,03	0,02	0,01	0,01	0,00	0,00	0,00	0,01	0,01	0,02
Al	1,37	1,39	1,26	13,76	14,39	14,38	15,61	10,30	10,30	9,04	9,02	10,02	0,02	0,01
Fe^{3+}	4,65	4,55	4,98	1,87	1,26	1,21	0,28	1,75	1,74	1,56	1,64	1,55	0,01	0,01
Fe^{2+}	10,98	11,08	10,98	3,01	2,02	2,13	4,90	3,14	3,21	3,25	3,32	3,37	1,35	1,35
Mg	1,78	1,69	1,67	5,12	6,13	6,06	3,10	5,09	5,01	4,89	4,83	4,76	0,61	0,62
Ca	0,05	0,07	0,04	0,00	0,01	0,00	0,01	0,00	0,01	0,01	0,00	0,00	0,00	0,01
Ti	4,95	5,00	4,86	0,17	0,15	0,18	0,05	0,24	0,25	0,15	0,16	0,15	1,97	1,97
Mn	0,17	0,17	0,19	0,05	0,01	0,01	0,05	0,03	0,02	0,01	0,01	0,03	0,02	0,02
Cr	0,02	0,01	0,00	0,01	0,00	0,01	0,00	3,44	3,46	5,09	5,02	4,11	0,00	0,00
Total	24,00	24,00	24,00	24,00	24,00	24,00	24,00	24,00	24,00	24,00	24,00	24,00	4,00	4,00
Fe^2O^3	21,76	20,98	22,75	11,75	8,20	7,89	1,74	10,15	10,02	8,79	9,20	8,82	0,20	0,26
FeO	46,20	45,99	45,16	16,96	11,81	12,44	27,08	16,37	16,69	16,42	16,77	17,28	33,10	32,91
Mg#	10	10	9	51	65	64	37	51	50	50	49	49	31	31
Cr#=Cr/(Cr+Al)	0,015	0,007	0,003	0,001	0,000	0,000	0,000	0,250	0,252	0,360	0,358	0,291	0,024	0,117
$Fe^{2+}/(Mg+Fe^{2+})$	0,860	0,867	0,868	0,370	0,248	0,260	0,613	0,382	0,391	0,399	0,407	0,414	0,688	0,686
$Fe^{3+}/(Cr+Al+Fe^{3+})$	0,769	0,765	0,798	0,120	0,081	0,078	0,018	0,113	0,112	0,100	0,104	0,099	0,233	0,377

c: core, mc: microcrystal, mp: microphenocryst, inc: inclusion

(BII)
ite
c
#160
0,02
0,35
33,97
7,93
0,01
52,94
0,40
0,05
95,67
J
0,00
0,02
0,04
1,37
0,59
0,00
1,98
0,02
0,00
4,01
0,98
33,08
29
0,088
0,700
0,618

Glass	Wehrlite (BII)				Phl-clinopyroxenite						Cpx-hornblendite (BII)									Hornblendite (BIII)				Hbl-Gabbro (BIII)			
Sample	K97-10a2				70a2						48a2			30a						17a2				42a2			
	Gim	Gim	Gp	Gp	Gim	Gim	Gim	Gim	Gim	Gim	Gp	Gp	Gim	Gim	Gim	Gim	Gim	Gim	inc (Hyn)	Gp	Gp	Gim	Gim	Gim	Gim	Gp	inc (Pl)
wt.%	#62	#63	#66	#74	#8	#9	#14	#19	#24	#25	#138	#144	#153	#6	#11	#15	#24	#102	#106	#27	#29	#36	#41	#44	#53	#56	#71
SiO_2	44,33	45,04	44,96	45,25	46,18	44,75	47,46	44,64	44,05	46,22	45,49	46,00	52,54	49,91	49,76	49,81	49,17	49,20	48,86	50,58	49,91	49,91	50,24	55,31	55,63	54,58	56,04
TiO_2	2,02	1,96	1,89	1,94	0,85	1,81	0,55	2,67	2,40	1,80	2,18	1,79	0,77	1,33	1,44	1,43	1,68	1,53	1,46	1,27	1,32	1,37	1,34	0,81	0,95	1,01	0,94
Al_2O_3	20,86	21,12	21,25	21,09	29,38	25,27	17,51	17,22	22,97	13,67	20,31	21,04	22,85	20,42	20,68	20,93	20,63	20,68	20,29	20,18	20,00	19,98	20,08	21,88	22,57	22,08	22,09
Fe_2O_3	8,06	7,33	7,47	7,67	3,35	5,22	7,91	9,77	8,20	8,87	5,22	4,46	3,37	6,64	7,42	7,54	6,82	7,23	7,42	6,58	7,38	6,98	7,00	4,25	4,46	4,62	4,38
MnO	0,18	0,19	0,16	0,13	0,16	0,21	0,26	0,26	0,26	0,28	0,21	0,14	0,00	0,17	0,17	0,17	0,14	0,17	0,20	0,15	0,18	0,17	0,16	0,15	0,13	0,14	0,10
MgO	3,48	3,33	3,11	2,94	1,25	2,40	5,13	5,31	2,48	7,19	5,01	4,59	1,42	2,32	2,48	2,35	2,58	2,11	2,65	2,32	2,63	2,57	2,76	1,08	0,98	1,11	1,03
CaO	8,55	8,11	8,00	7,65	4,30	5,92	11,81	11,26	5,60	15,00	9,27	9,07	5,36	6,99	6,89	5,66	6,86	5,93	6,95	5,40	6,00	5,81	5,86	2,88	2,51	2,72	2,43
Na_2O	6,04	6,41	6,55	6,41	9,46	9,86	3,59	2,94	9,17	6,33	9,67	10,70	9,88	5,27	5,15	5,37	5,84	4,44	5,34	5,38	5,33	5,28	5,23	5,53	5,46	5,54	5,66
K_2O	3,58	3,55	3,86	3,93	3,33	2,93	3,03	5,84	3,31	1,71	1,72	1,64	2,74	4,17	3,92	3,97	4,21	3,49	3,74	4,81	4,47	4,65	4,76	5,49	5,52	5,44	5,51
P_2O_5					0,40	0,45	0,54	0,49	0,35	0,59																	
Total	97,1	97,0	97,2	97,0	98,7	98,8	97,8	100,4	98,8	101,6	99,1	99,4	98,9	97,2	97,9	97,2	97,9	94,8	96,9	96,7	97,2	96,7	97,4	97,4	98,2	97,2	98,2
FeO_t	7,3	6,6	6,7	6,9	3,0	4,7	7,1	8,8	7,4	8,0	4,7	4,0	3,0	6,0	6,7	6,8	6,1	6,5	6,7	5,9	6,6	6,3	6,3	3,8	4,0	4,2	3,9
Mg#	44	45	43	41	40	45	54	49	35	59	63	65	43	38	37	36	40	34	39	39	39	40	41	31	28	30	30

Gp: glass pockets, Gim: glass associated with intergranular minerals, inc: inclusion, Hyn: hauyne, Pl: plagioclase.Hbl: hornblend, Cpx: clinopyroxene, Phl: phlogopite

Equation (13) Putirka RiMG '08 T(C)	Equation (14) Putirka RiMG '08 T(C)	Equation (15) Putirka RiMG '08 T(C)	Equation (16) Putirka RiMG '08 T(C)	Helz & Thornber '87 Mg-thermometer T(C)
1086	1143	1169	1163	1084
1086	1143	1180	1187	1084
1086	1143	1180	1187	1084
1086	1143	1180	1187	1084
1082	1140	1166	1147	1081
1082	1140	1178	1170	1081
1082	1140	1178	1170	1081
1082	1140	1178	1170	1081
1076	1139	1161	1142	1077
1076	1139	1173	1166	1077
1076	1139	1173	1166	1077
1076	1139	1173	1166	1077
1072	1131	1154	1131	1073
1072	1131	1166	1155	1073
1072	1131	1166	1155	1073
1072	1131	1166	1155	1073

Helz & Thornber '87 Ca-thermometer T(C)
1110
1110
1110
1110
1103
1103
1103
1103
1101
1101
1101
1101
1095
1095
1095
1095

	Host rock									Enclave							
Sample-K97-	BI	BII	BIII							Wehrlite	Phl-Cpxt	Cpx-Hornblendite		Hornblendite		Plb Cpx-Hblt	Hbl-Gabbro
wt.%	58	30	31	48	14	17	42	46	70	10a2	70a2	30a	48a2	14a	17a2	46a	42a2
SiO_2	46,04	47,12	45,49	45,22	47,05	47,45	46,94	47,44	47,01	42,05	40,45	41,69	39,12	38,94	38,92	41,39	44,83
Al_2O_3	15,59	17,54	16,81	17,19	17,92	17,89	17,69	18,18	17,84	3,82	12,1	15,32	14,6	15,25	14,8	15,55	17,66
Fe_2O_3	8,69	8,76	8,98	9,31	8,5	8,21	8,65	8,31	8,01	12,16	9,3	10,13	12,34	11,1	11,05	9,83	9,24
MnO	0,13	0,16	0,16	0,17	0,15	0,14	0,15	0,16	0,14	0,17	0,15	0,14	0,21	0,15	0,13	0,13	0,16
MgO	7,22	5,78	7,7	6,07	5,94	6,1	6,52	5,4	5,71	34,63	12,1	10,4	11,57	8,8	11,38	10,66	6,34
CaO	10,95	8,48	9,24	8,89	8,31	7,88	8,65	8,01	7,89	7,35	13,76	12,72	12,77	13,15	12,69	11,88	9,95
Na_2O	3,36	5,37	5,15	5,09	5,77	5,68	5,53	5,93	5,69	0,53	1,53	3,37	2,73	3,3	2,89	3,25	4,87
K_2O	2,37	3,21	3,19	3,3	3,55	3,62	3,55	3,55	3,57	0,31	4,16	1,85	1,52	2,39	1,94	2,06	2,74
TiO_2	2,05	1,96	2,07	2,32	1,9	1,81	1,99	1,89	1,77	0,75	3,12	3,11	4,14	3,3	4,19	3,89	2,53
P_2O_5	0,69	0,99	1	0,75	0,85	0,86	0,88	0,9	0,82	0,12	1,76	0,79	0,26	2,82	1,48	0,62	1,18
LOI	1,93	0,42	0,2	1,05	-0,03	0,58	-0,18	0,06	0,19	-0,41	1,95	0,73	0,49	0,51	0,47	0,62	0,32
TOTAL	99,02	99,79	99,99	99,36	99,91	100,22	100,37	99,83	98,64	101,48	100,38	100,25	99,75	99,71	99,94	99,88	99,82
(ppm)																	
Sr			1101				980		998	159	1149	1609	1041	1049	1022	1019	1256
Ba			956				940		881	86	2771	761	804	852	768	819	951
Rb			74,7				72,9		84,5	4,9	109	23,1	7	34,7	21,3	19,9	47,9
Ni			69				55		50	598	91	23	13	< .5	39	39	18
Co			34,2				35,9		37,2	117,8	41,5	53	69,5	48,5	58,6	50,7	38,2
Cr	182	141	167	94	113	68	78	68	59	2331	301	96	34	7	42	94	68
V			195				169		149	115	329	349	437	293	382	372	234
Zr	260	301	230	273	239	239	242	254	227	35	303	261	193	205	189	228	252
Y			27,4				25,1		26,2	6,2	24,9	27,3	28,8	37,2	33,2	29,8	31,7
Nb			86,8				81,9		93,8	10,8	79,2	61	63,5	73,1	66,2	65,2	93,1
Ga			20,7				20,6		22,8	6	18,5	17,9	19,1	18,3	17,2	17,7	20,7
Cs			1,1				1,2		1,4	< .1	1,3	0,2	< .1	0,4	0,2	0,3	0,7
Hf			4,4				4,4		5,5	1,2	7,7	4,6	4,1	4,3	4,6	4,9	5,2
Ta			5,3				5		5,1	0,9	4,2	3,3	3,2	4,4	4,3	4,1	5,5
Th			8,2				8,3		8,3	0,7	6	5,6	0,7	4,5	2,4	3,4	6,9
Tl			0,3				0,1		< .1	0,4	0,2	0,2	0,1	0,2	0,4	0,1	0,3
U			2,8				1,8		2,8	0,5	1,1	2	0,1	1,6	0,6	0,9	2,6
Zr			209,8				199,8		229,5	40,2	280,8	175,7	144,4	154	134,4	175,2	226,2
La			59				52,1		53,9	8,1	81,2	50,7	33,9	61,5	40,3	37	68,8
Ce			100,7				88,3		89,5	17,4	162,5	109,5	75,5	117,1	85,4	74,6	117,3
Pr			10,55				9,2		9,68	2,28	18,98	14	9,37	13,69	10,88	8,64	12,26
Nd			45,5				38,8		36,2	11	82,8	65,2	42,7	59,6	50,1	40,9	49
Sm			7,2				6,2		6,2	2,1	13,2	11,1	7,9	11,1	9,5	8	8
Eu			2,29				2,03		2,07	0,78	3,58	3,26	2,7	3,69	3,08	2,68	2,69
Gd			6,62				5,78		5,74	1,86	10,22	8,05	8,03	10,63	9,52	8,03	7,98
Tb			0,95				0,87		0,81	0,26	1,21	1,07	1,06	1,34	1,27	1,12	1,06
Dy			5,19				4,66		5,08	1,37	5,73	5,54	5,56	7,23	6,72	6,1	6,09
Ho			0,95				0,86		0,9	0,21	0,89	0,97	0,99	1,25	1,2	1,05	1,07
Er			2,47				2,32		2,55	0,59	2,15	2,58	2,55	3,26	2,92	2,92	2,88
Tm			0,36				0,35		0,39	0,09	0,26	0,35	0,34	0,46	0,38	0,35	0,36
Yb			2,23				2,13		2,29	0,48	1,6	2,01	2,22	2,45	2,34	2	2,29
Lu			0,32				0,3		0,34	0,06	0,22	0,3	0,31	0,35	0,34	0,31	0,37
Pb			2				3		4	< 2	< 2	3	< 2	< 2	< 2	< 2	3

Cpx: clinopyroxene, Hbl: hornblende, Phl: phlogopite, Plb: plagioclase-bearing, Cpxt: clinopyroxenite , Hblt: hornblendite

			T°C		P(kbar)	
			min	max	min	max
Host rocks	BI	*Cpx-whole rock*	1217	1231	9,5	10,0
	BII		1130	1242	10,0	15,4
	BIII		1149	1227	9,5	14,3
	Bomb in M3 (BII)	*Cpx-coexisting glass*	1174	1260	13,0	19,5
Enclaves	Wehrlite (BII)	*Cpx-coexisting glass*	1138	1200	14,2	18,8
	Hornblendite (BII)	*Cpx-whole rock*	1259	1329	11,6	18,3
	Phlogopite clinopyroxenite (BIII)	*Cpx-whole rock*	1314	1324	14,1	15,5
		Cpx-coexisting glass	1148	1199	25,2	27,6
	Clinopyroxenite hornblendite (BII)	*Cpx-whole rock*	1221	1266	12,1	13,4
	Clinopyroxenite hornblendite (BII)	*Cpx-whole rock*	1277	1301	13,0	14,7
	Clinopyroxenite hornblendite (BII)	*Cpx-coexisting glass*	1134	1206	14,4	21,4
	Hornblende gabbro (BIII)	*Cpx-whole rock*	1208	1220	11,1	12,8
	Hornblende gabbro (BIII)	*Cpx-coexisting glass*	1026	1034	14,2	15,7